EARTH SURFACE PROCESSES AND LANDFORMS
Earth Surf. Process. Landforms (2019)

Published online in Wiley Online Library
(wileyonlinelibrary.com) DOI: 10.1002/esp.4589

Spatial variation of flow characteristics in a subarctic meandering river in ice-covered and open-channel conditions: A 2D hydrodynamic modelling approach

Eliisa Lotsari,[1,2]* Tiia Tarsa,[1] Maria Kämäri,[1,3] Petteri Alho[2,4] and Elina Kasvi[2]
[1] Department of Geographical and Historical Studies, University of Eastern Finland, Joensuu, Finland
[2] Department of Geography and Geology, University of Turku, Turku, Finland
[3] Finnish Environment Institute, Freshwater Centre, Helsinki, Finland
[4] Finnish Geospatial Research Institute, National Land Survey of Finland, Masala, Finland

Received 2 March 2018; Revised 11 January 2019; Accepted 17 January 2019

*Correspondence to: Eliisa Lotsari, Department of Geographical and Historical Studies, University of Eastern Finland, Yliopistokatu 2, P.O. Box 111, 80101 Joensuu, Finland. E-mail: eliisa.lotsari@uef.fi

ESPL
Earth Surface Processes and Landforms

ABSTRACT: To be able to understand year-round river channel evolution both at present and in the future, the spatial variation of the flow characteristics and their sediment transport capabilities under ice cover need to be detected. As the measurements done through cross-sectional drill holes cover only a small portion of the river channel area, the numerical simulations give insight into the wider spatial horizontal variation of the flow characteristics. Therefore, we simulate the ice-covered flow with a hydrodynamic two-dimensional (2D) model in a meandering subarctic river (Pulmanki River, Finland) in mid-winter conditions and compare them to the pre-winter open-channel low flow situation. Based on the simulations, which are calibrated with reference measurements, we aim to detect (1) how ice-covered mid-winter flow characteristics vary spatially and (2) the erosion and sedimentation potential of the ice-covered flow compared to open-channel conditions.

The 2D hydrodynamic model replicated the observed flow characteristics in both open-channel and ice-covered conditions. During both seasons, the greatest erosional forces locate in the shallow sections. The narrow, freely flowing channel area found in mid-winter cause the main differences in the spatial flow variation between seasons. Despite the causes of the horizontal recirculating flow structures being similar in both seasons, the structures formed in different locations depended on whether the river was open or ice covered. The critical thresholds for particle entrainment are exceeded more often in open-channel conditions than during ice-covered flow. The results indicate spatially extensive sediment transport in open-channel conditions, but that the spatial variability and differences in depositional and erosional locations increase in ice-covered conditions. Asymmetrical bends and straight reaches erode throughout the year, whereas symmetrical, smaller bends mainly erode in open-channel conditions and are prone to deposition in winter. The long ice-covered season can greatly affect the annual morphology of the submerged channel.

KEYWORDS: 2D model; hydrodynamics; ice-covered flow; meandering river; erosion

Introduction

The flow structure of meandering rivers is complex, particularly due to the curvature of the channel and the related interactions between flow and sediment dynamics. However, in cold river environments, the complexity of these process interactions increases when the flow is ice-covered for most of the year. In these high latitude areas, future climatic change has been forecast to increase winter temperatures [Intergovernmental Panel on Climate Change (IPCC), 2013; 2018]. Trends indicate later freeze dates for rivers and lakes in the Northern Hemisphere, with breakup dates being 6.5 days earlier on average compared to 100 years earlier (Magnuson *et al.,* 2000). Climate change may reduce ice breakup intensity and ice-induced flooding, which may have further ecological consequences, such as changes in riparian vegetation (Lind *et al.,* 2014). Thus, changes in flow, ice and sediment transport conditions can have complex influences on the environment.

Before being able to understand river channel evolution in the future, the present ice-covered flow conditions need to be understood in these areas, such as in subarctic northern Finland, where rivers have ice cover *c.* 7–8 months of the year (Lotsari *et al.,* 2015). Even though ice-covered flow has been studied since the beginning of the twentieth century (Barrows and Horton, 1907), so far mainly laboratory studies of ice-covered flow and sediment transport have been published (Sayre and Song, 1979; Lau and Krishnappan, 1985; Urroz and Ettema, 1994; Tsai and Ettema, 1994, 1996; Smith and

Ettema, 1995; Ettema *et al.,* 2000; Wang *et al.,* 2008; Sui *et al.,* 2010). Only three recent field studies (Demers *et al.,* 2011, 2013; Lotsari *et al.,* 2017) have analysed the effects of ice on flow in meandering rivers, despite the fact that concerns regarding the insufficient understanding of the processes under ice-covered conditions have existed for decades (Ettema, 2002; Turcotte *et al.,* 2011). In particular, some processes have only been known conceptually (e.g. altered bedform geometry) and others have been barely recognized (e.g. channel-thalweg adjustment: Ettema, 2002; Turcotte *et al.,* 2011). The recent studies have shown, most importantly, that two vertically stacked helical flow cells (instead of one) can appear under ice and the direction of the flow is opposite to the open-channel measurement conditions (Demers *et al.,* 2011; Lotsari *et al.,* 2017). These results are similar to those of Urroz and Ettema (1994), who had observed this in laboratory conditions. As the friction caused by ice-cover moves the high velocities deeper, when compared to ice-free conditions, top- and bottom-layer flows are also directed (around the apex area) toward the opposite direction to the maximum velocities occurring in the middle flow layers (Demers *et al.,* 2011; Lotsari *et al.,* 2017). According to Lotsari *et al.* (2017), increased erosion in the riffle areas and deposition in pool/thalweg areas are expected during ice-covered conditions due to these changes in vertical velocity distribution. Thus, the impact of long-term changes (i.e. warming) in winter temperatures could be great on seasonal erosion conditions.

Previous studies have also hinted, based on measurements taken through drill holes, that ice cover affects the horizontal variation of flow, especially in bends (Demers *et al.,* 2011; Lotsari *et al.,* 2017). So far it has been possible to show that despite the shifting of the high velocity core (HVC) from one side of the channel to the other, and the presence of back eddies under both open-channel and ice-covered conditions, differences also exist (Kasvi *et al.,* 2013b; Kämäri *et al.,* 2017; Lotsari *et al.,* 2017). The location of the HVC under ice varies more between consecutive cross-sections than in ice-free conditions (Lotsari *et al.,* 2017). In ice-free conditions the HVC locates next to the inner bank at upstream cross-sections, moves towards the outer bank around the apex, and then follows the thalweg in the downstream cross-sections of a meander bend. In addition, under ice, velocities are particularly reduced when entering deeper water downstream of the apex of meander bends (Lotsari *et al.,* 2017). However, these studies were mainly able to show vertical flow characteristics and not the horizontal flow structures within the channel in open-channel and ice-covered flow conditions.

In addition, ice cover has been also observed to reduce turbidities when compared to the open-channel conditions of equivalent discharges (Kämäri *et al.,* 2015, 2018). However, Turcotte and Morse (2017) have observed both lower or higher turbidities in ice-covered channels than in open-channel conditions. While the spring snow-melt flood and ice breakup periods may be major sediment transport events and may also be when the greatest annual turbidities occur (Turcotte *et al.,* 2011; Turcotte and Morse, 2017), the other seasons (including mid-winter, where there are ice-covered low flows) may cause great total channel changes (Lotsari *et al.,* 2014a). In subarctic sand-/gravel-bed rivers, earlier studies have shown the whole open-channel low flow period (i.e. 3–4 months) to cause more sediment transport than the snow-melt flood (*c.* 10 days), which is shorter in duration (Lotsari *et al.,* 2014b). However, the sediment transport potential and its spatial distribution during conditions of mid-winter stable floating ice cover have not received much attention (Turcotte *et al.,* 2011). Recent studies based on velocity observations in a subarctic meandering river have implied that there could be increased erosion in the riffle areas and deposition in pool/thalweg areas during ice-covered conditions (Lotsari *et al.,* 2017). However, these processes need further examination. Before being able to analyse channel erosion under ice-covered conditions in detail, the first step is to analyse in more detail the spatial variation of flow characteristics and their potential capabilities for transporting sediment. The point measurements of previous studies (e.g. Demers *et al.,* 2011; Lotsari *et al.,* 2017) represent only narrow areas within the channel and the wider spatial flow distribution and its effects on erosion–sedimentation potential are yet to be resolved.

During the last couple of decades, enhancements in methods for analysing these processes have taken place, particularly with regard to flow measurement techniques (Demers *et al.,* 2011) and modelling approaches (Waddle, 2007). Despite Acoustic Doppler Current Profiler (ADCP) or Acoustic Doppler Velocimeter (ADV) sensors enabling ice-covered flow measurements throughout the vertical water column when used through drill holes, the measurements are still mainly made cross-sectionally, whereas in open channel flow conditions it is possible to acquire measurements at a much greater spatial density, for example, by installing the ADCP on a remote-controlled platform (Kasvi *et al.,* 2017). As measurements undertaken through cross-sectional drill holes cover only a small portion of the river channel area, numerical simulations – calibrated based on the more limited measurement data – could give insight into the spatial variation of flow characteristics more widely. One-dimensional (1D) unsteady flow models have been applied for ice-covered flow detection since the mid-1980s (Yapa and Shen, 1986; US Army, 1998; Lal and Shen, 1991; Kämäri *et al.,* 2015). However, the models and analyses undertaken in ice-covered rivers have been mainly undertaken based on laboratory/flume experiments (Urroz and Ettema, 1994; Tan *et al.,* 1998). Numerical two-dimensional (2D) hydrodynamic simulations (Vietz *et al.,* 2012) and three-dimensional (3D) hydrodynamic simulations have been used in meandering rivers in open-channel conditions (Kasvi *et al.,* 2015) and for analysing ecohydraulics (Fukuda *et al.,* 2015), but not for the ice-covered conditions of a subarctic meandering river. To be able to detect the 3D vertical flow structure in meander bends, 3D simulations are needed. However, the first step is to detect the performance of a simpler 2D model and see whether it can simulate the spatial variation of flow characteristics in an ice-covered meandering river where stable ice cover is present in mid-winter conditions. The ice-covered flow characteristics need to be compared to open-channel flow more thoroughly. The modelling also enables the highly needed studies of flow characteristics of multiple consecutive meander bends (Demers *et al.,* 2011; Lotsari *et al.,* 2017).

Therefore, as a continuation of the preceding studies by Lotsari *et al.* (2017) and Kämäri *et al.* (2017), who studied ice-covered (mainly vertical) flow and river ice cover based on measurements, we will simulate both the mid-winter ice-covered low flow and the preceding autumn open-channel low flow conditions for the same subarctic river. Based on the simulation approaches, which are calibrated using reference measurements, we aim to detect (1) how ice-covered mid-winter flow characteristics vary spatially and (2) the erosion and sedimentation potential of the ice-covered flow compared to open-channel conditions. The study will cover three meander bends and one straight reach between these bends of the Pulmanki River, northern Finland. The study will be based on both a hydrodynamic 2D model (River2D: University of Alberta, http://www.river2d.ualberta.ca/: Steffler and Blackburn, 2002) and reference measurements of flow,

sediment characteristics, topography and ice cover. The hypotheses are that (1) the ice-covered flow characteristics are spatially more variable than during the open-channel conditions and (2) there is great difference in erosion and sedimentation locations between the seasons, although the overall sediment transport potential is lower during the ice-covered mid-winter conditions.

Study Area

The study area is located in the lowest reach of the upper Pulmanki River (northern Finland), which drains first into Lake Pulmanki and then into the Tana River. The reach consists of three meander bends and one straight reach between two of the bends (Figure 1). The river normally freezes in October, and the ice cover lasts until the snow-melt period (from mid-May to early June). Depending on the year, there can be 0 to 30 cm of snow on the river ice. Summer discharges are typically low (4 m^3/s) compared with spring (50 m^3/s) (Kasvi *et al.,* 2013b). In autumn and winter the discharges can be less than 2 m^3/s (Lotsari *et al.,* 2017). Thus, this river represents a typical subarctic river with its flow characteristics and ice cover processes.

The freezing processes and channel slope are similar throughout the *c.* 1200 m long study reach and no rapids, anchor ice, frazil ice or hanging dams occurred in 2013–2014 (i.e. within the measurement period of this study). In general, the ice formation started as border or shore ice growth along the riverbanks (cf. Beltaos, 2013), followed by local ice bridging and thin ice cover (i.e. skim-ice formation) (Kämäri *et al.,* 2017). Localized border ice growth presumably also occurred during the freeze-up period along the sandy bars (Kämäri *et al.,* 2017). Kämäri *et al.* (2017) estimated that skim ice formed on the Pulmanki River when the cumulative number of freezing air temperature degree-days was 22 (e.g. on 21 October 2013). The ice type of the Pulmanki River was visually inspected from boreholes, the bottom layer of ice was defined as 'crystal clear black ice', and the top of the ice (a 10–20 cm thick layer) was 'white-coloured snow ice'. The ice roughness was defined visually as smooth–rough, similar to the approach of Lotsari *et al.* (2017) and Kämäri *et al.* (2017), who in turn had followed the definition of Demers *et al.* (2013).

The studied reach was selected due to the different characteristics of its bends (Figure 1; Lotsari *et al.,* 2014a). Bend 1 is asymmetrical, but the other bends are symmetrical in their shape. The river is mainly in its natural state, except that the outer bank of Bend 1 has rip-rap erosion protection. The inner banks of all bends have non-vegetated point bars, but the outer banks of Bends 2 and 3 are vegetated. The low flow sub-water channel area is free of vegetation and consists of highly mobile sand and gravel. There is no bed armour layer formed in the study reach and mid-channel bars are gradually prograding along the river-bed (cf. aerial photos from Kasvi *et al.,* 2017).

Due to the annually challenging winter conditions, it was only possible to measure the suspended sediment and bedload transport in February 2017. Discharge was, on average, 1.1 m^3/s at that time, based on three cross-sectional measurements. Note that this was almost double compared to the flow for the 2014 winter period (cf. Table I). Despite the different discharge conditions, the sediment transport measurements of February 2017 justify the possibility of sediment transport, that is to say, the exceedance of the critical velocities, in ice-covered mid-

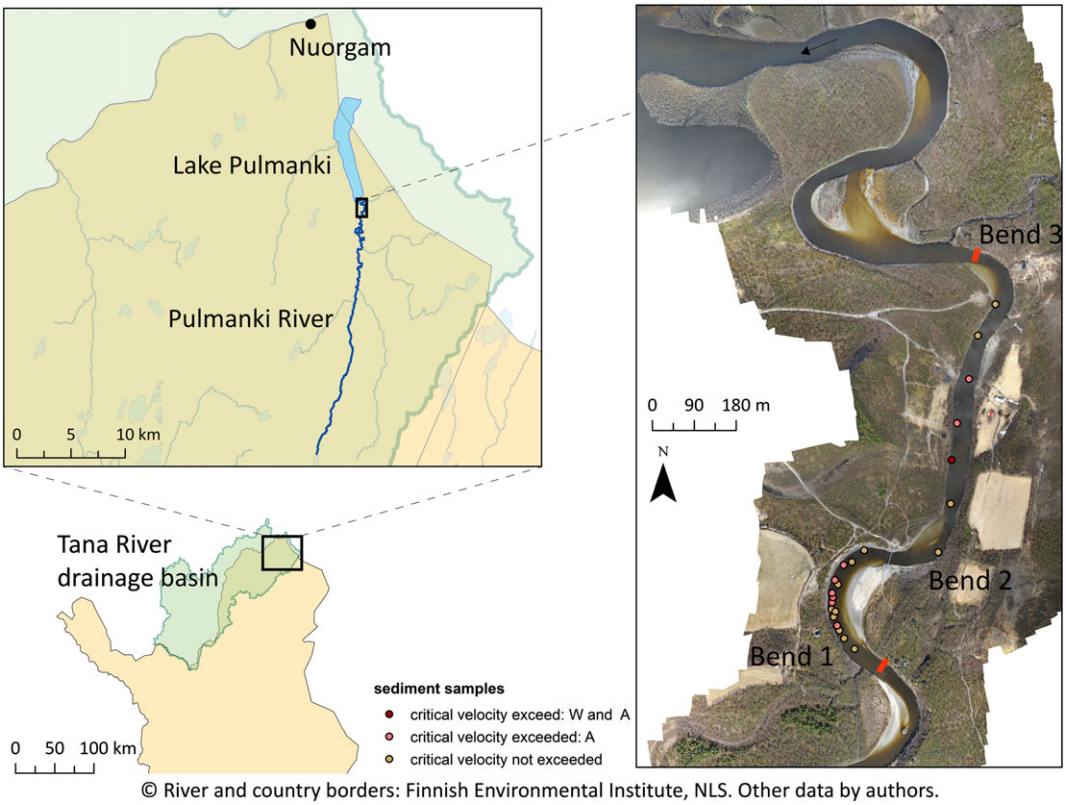

Figure 1. The Pulmanki River study site locates in northern Finland, and it consists of three meander bends and one straight reach. The straight lines (in right hand side figure) mark the upstream and downstream boundaries of the study site. The upstream part of Tana River watershed is shown, i.e. upstream of the confluence of Pulmanki and Tana Rivers. The sediment sample locations are also shown. The exceedance of the critical velocity was analysed (W = winter, A = autumn: cf. results section). The aerial photograph is from May 2018 and taken by Eliisa Lotsari. [Colour figure can be viewed at wileyonlinelibrary.com]

Table I. The discharges used in the modelling

Date	Q (m^3/s)	Sensor	Water/ice surface (m above sea level)	Application	Notes
2 June 2013	5.10	ADCP	14.580 (water)	Verification: open-channel model	Q was based on rating curve, only W was measured
5 September 2013	1.71	ADV	13.951 (water)	Calibration: open-channel model	Q and W were measured
3 March 2014	0.63	ADCP	14.412 (ice)	Calibration: ice-covered model	Q and W were measured

Note: Q, discharge (m^3/s); W, water level (in metres). ADCP, Acoustic Doppler Current Profiler; ADV, Acoustic Doppler Velocimeter.

winter conditions. Four depth-integrated water samples (Rickly DH-48) had been taken simultaneously with 6 min long Helley–Smith bedload samples from the middle section of the straight reach between Bends 2 and 3. The water samples for suspended sediment analyses were collected by slowly lowering the sampler through the water column. The water sample sizes were *c.* 0.45 l. These samples were vacuum filtered by applying filters having 0.45 µm pore sizes. The filters had been dried and weighed before the filtering. This was done also after filtering to calculate the total suspended solids (TSS). TSS transport was then up to 0.67 mg/l and bedload transport was 22.84 mg/m/s. The D_{50} grain size of the measured bedload was 0.5 mm, based on dry sieving.

The annual vertical channel change in the sand-bed meander bends has been observed to be as great as ±70 cm (Vaaja *et al.,* 2011). The lateral shift varies, but *c.* 0.5 m annual rates have been observed in higher banks, upstream of this present study site (Lotsari *et al.,* 2014a). Historical oxbow lakes indicate multiple meander cutoffs within the river valley during the last 600 years (Mansikkaniemi and Mäki, 1990). The spring snow-melt high flow period has been shown to be the greatest single channel-forming event in the Pulmanki River (Kasvi *et al.,* 2013a, 2013b; Lotsari *et al.,* 2014a), when water stages 2.5 m higher than the summer season are reached (Lotsari *et al.,* 2014a). However, slower changes in the meandering channel and associated point bars may also occur during low-flow periods in autumn and winter. Only the spring floods can reach the top of the point bars as the point bars and mid-channel bars are above the water level in the autumn and winter low flow periods. Thus, the erosion due to fluvial processes concentrates in different river sections during high and low flow periods. However, the spatial variation of the magnitudes of fluvial processes (and therefore also of river erosion and sedimentation) during these low flow periods is yet to be revealed by the present study.

Data and Methods

Channel and ice-cover topographies

The topography of the sub-water areas was measured with the ADCP in spring (May) 2013 open-channel flow conditions and autumn (September) 2013 open-channel flow conditions.

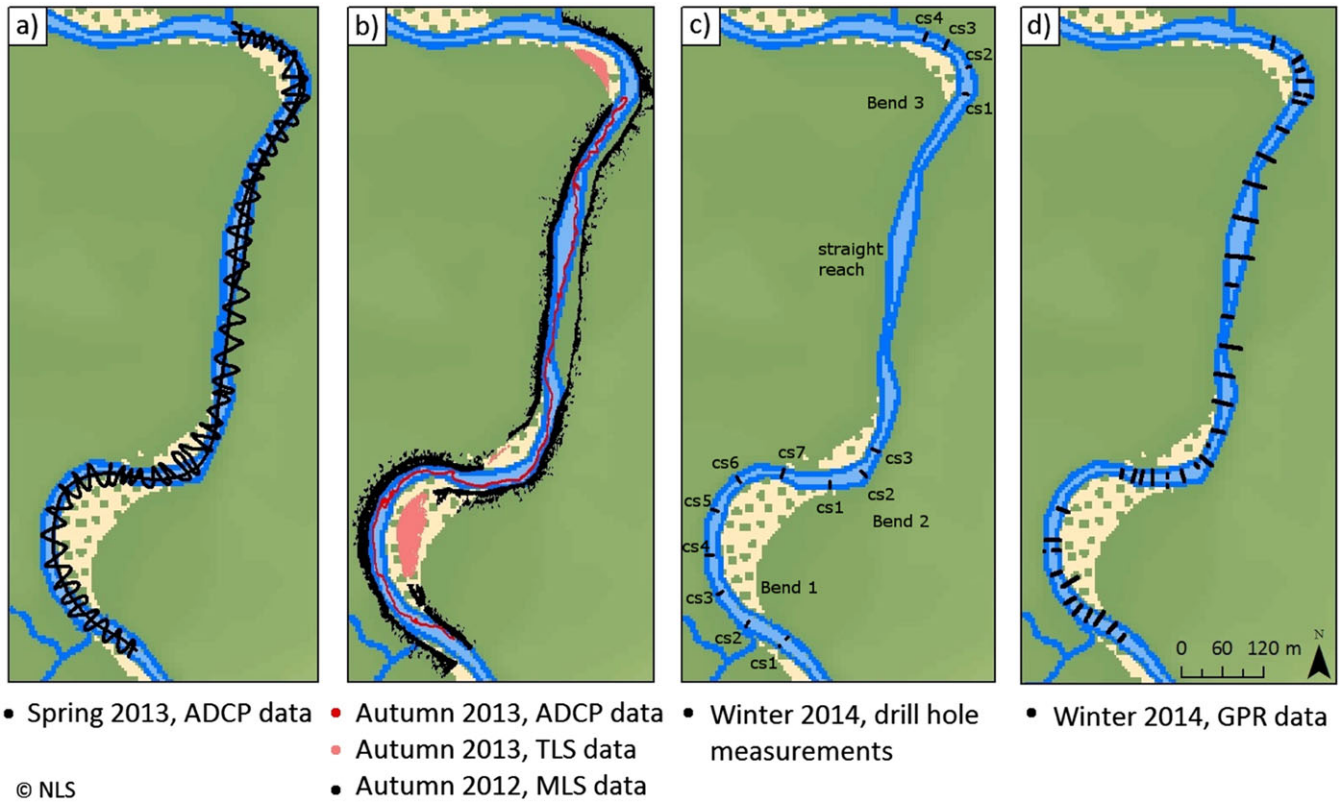

Figure 2. The Acoustic Doppler Current profiler (ADCP), laser scanning and ground penetration radar (GPR) measurements during the study period. [Colour figure can be viewed at wileyonlinelibrary.com]

The Sontek M9 sensor was installed in a remote controlled mini-boat for measurements. The vertical beam (0.5 MHz) of the sensor was used for echo sounding the bed elevation. According to the manufacturer (Sontek, 2018), the accuracy of the depth measurement is 1%.

In addition to this pre-winter topography, the winter 2014 (February/March) river-bed elevations were measured through drilled holes. The ADCP sensor was deployed through these holes which were 1 m apart from each other along the cross-sections. The stationary measurement mode was used. The winter 2014 cross-sectional topographical measurements were added to the pre-winter topography (Figure 2c) and the river-ed topography was modified to resemble the ice-covered conditions as well as possible.

The ice-covered flow model also requires the ice topography, in other words, the ice–water interface elevations (IWIEs) and the ice surface elevations (ISEs). These measurements included the manual ice thickness measurements and RTK-GNSS (real-time kinematic global navigation satellite system) measurements of the ISEs at the drill holes of the ADCP (Figure 2c). In addition, the ice thickness variation over a large number of cross-sections was gained using ground penetrating radar (GPR), specifically a Malå 800 MHz sensor (Figure 2d). The GPR measurements were verified based on the manual ice-thickness measurements, which were done from the same drill holes as those through which the ADCP was applied (Kämäri *et al.,* 2017).

The spring (May) 2013 topography data was applied to the autumn (September) 2013 topography, and the application of these spring and autumn data to the winter (February/March) 2014 topography was justified by analysing the resemblance of the river-bed elevations between these measurement time steps. The spring 2013 bed elevations were compared to the autumn 2013 and winter 2014 bed elevations. In addition, the autumn 2013 values were compared to winter 2014 values. Because there was a slight difference in the measurement location between the measurement time steps, the closest points between the compared time steps were selected for analyses. No more than 50 cm horizontal difference between the point pairs was allowed. After the pairs had been defined, the elevation differences were analysed with a paired sample *t*-test. The test assumes that the difference of each value pair follows a normal distribution (Wilcox, 2009). This normal distribution was tested with the Shapiro–Wilk test (Shapiro and Wilk, 1965). In all of the cases, the differences of the value pairs followed a normal distribution.

When the spring 2013 and winter 2014 bed elevations were compared, altogether 12 elevation point pairs were selected. The paired sample *t*-test showed that there was no statistically significant difference (p = 0.06404) between the elevations between the different time steps. When the spring 2013 and autumn 2013 values were compared, 10 pairs were evaluated. Similarly, there was no statistically significant difference between the spring 2013 and autumn 2013 bed elevations (p = 0.05939). When the autumn 2013 and winter 2014 bed elevations were compared, 14 pairs of measurement values were applied. The *t*-test again showed that there was no statistically significant difference between the river-bed elevations (p = 0.1827). The zero-hypothesis was that the values do not differ from each other (when $p < 0.05$, the values differ from each other significantly).

Flow measurements

Water level, flow characteristics and discharges were measured for modelling purposes. The water depth was measured every 15 minutes with a Solinst Levelogger sensor, which had been installed for the 2013 open-channel flow period at Bend 3. A reference water level was measured from the depth sensor locations with the RTK-GNSS. The winter water depth was defined along with the ADCP and IWIE measurements (see previous section).

The ADCP measurements recorded the flow velocity and direction throughout the water column in addition to the water depth and channel bed topography (cf. previous section). The sensor applies 3.0/1.0 MHz beams, depending on the water depth in question. According to the manufacturer (Sontek, 2018), the accuracy of the velocity measurements is ±0.25 % of the measured velocity. The ADCP flow measurements of autumn 2013 were taken along the thalweg, but the winter measurements were cross-sectional. The depth-averaged velocities of the measurements were applied for calibrating the model (see the following sections). From the cross-sectional winter

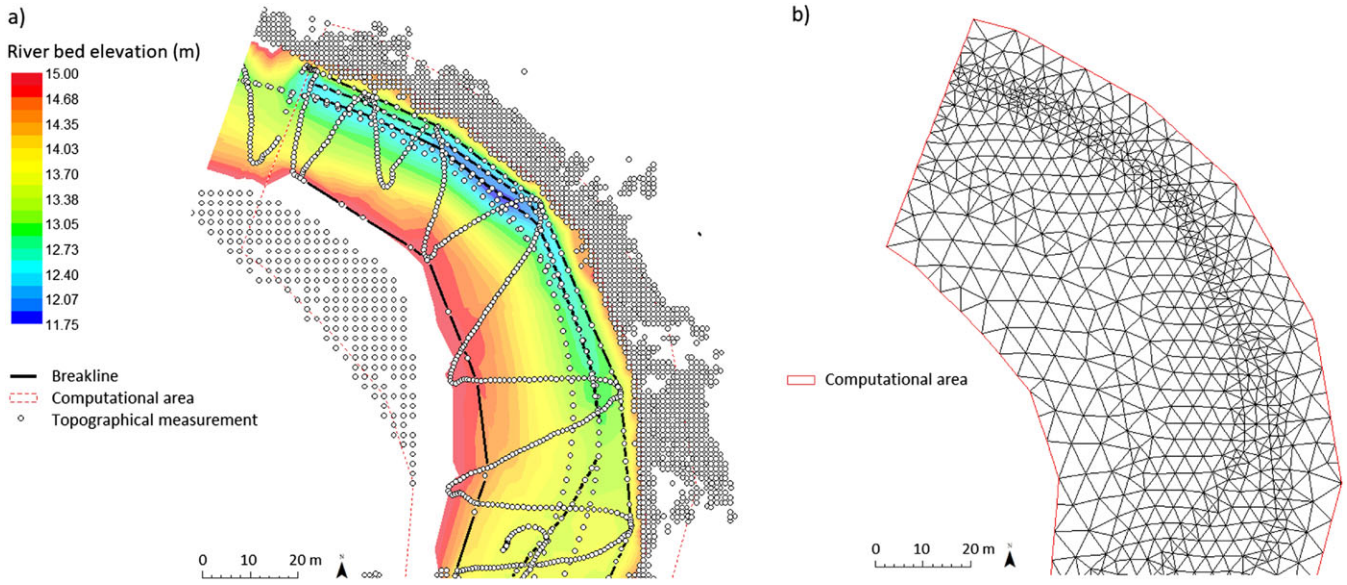

Figure 3. (a) The final triangulated irregular network (TIN) geometry after the enhancement of the topography by creating the breaklines of deeper areas and the shorelines. (b) The mesh, which was created from the TIN model. The examples are from the open-channel flow model of Bend 3. [Colour figure can be viewed at wileyonlinelibrary.com]

measurements, the highest velocity measurement locations of each cross-section were also compared to the simulation results.

The discharges applied for the 2D hydrodynamic model were measured with the ADCP in spring 2013 and winter 2014 (see Table I). In ice-covered flow conditions, the discharge was measured from the same cross-sections as those from which the winter topography was measured. During the low water period of autumn 2013, that is, when wide areas had depths of less than 0.2 m, the discharges were measured using an ADV (see Table I). The station interval along the cross-section was 2 m in the ADV measurements.

The 2D hydrodynamic models and their geometries

The depth-averaged hydrodynamic River2D model, which is capable of simulating 2D flow vectors that allow the direction and magnitude of the time- and depth-averaged, spatially recirculating flow structures (RFSs) to be defined, was applied (Vietz *et al.,* 2012). Two model set-ups were employed: (1) one with the open-channel topography (2013, pre-winter), (2) and the other with the ice-covered topography (2014, February/March). In both cases, the topographical measurements were imported in the model as points, and then a triangulated irregular network (TIN) was formed (Figure 3). The TIN was further enhanced by creating contour breaklines in the deeper areas and shoreline (i.e. in the highest sub-water topography elevations). Finally, a finite element mesh of the topography was created based on the TINs. The density of mesh nodes was the greatest in the submerged areas and where great topographical changes occurred.

The same simulation area extent was defined for both the open-channel and ice-covered models. The computational areas started from the downstream side of the upstream-most winter (February/March 2014) cross-section measured and ended at the upstream side of the downstream-most winter cross-section measured. This domain was selected because the mesh creation and the simulation results are best (Blackburn and Unterschultz, 2002) when topographical observations exist upstream and downstream of the computational area.

For the ice-covered flow model, the ice topography included the ice thickness and its roughness (defined as Manning' *n*-value; see the detailed description of the calibration later) at each location, being based on the manual and GPR measurements. All together 14 303 ice cover points were fed into the model. Only in two locations, where the ice thickness was zero, did open flow conditions prevail. These were the left bank side measurement location of the two upstream-most cross-sections. Because the upstream-most cross-section was not included in the computational area, only one open-channel measurement location was included in the winter model. The breaklines were applied around these measurement points.

The calibration of the open-channel flow model

Both of the models (i.e. one with a pre-winter open-channel topography and one with a winter ice-covered topography) were calibrated separately and followed the standard procedure for sensitivity tests in order to adjust roughness parameters. The discharges were applied as the upstream boundary condition. The corresponding water level was used as the downstream boundary condition of the open-channel flow model, and the ISE was used as the downstream boundary condition in the ice-covered flow model (Table I).

The open-channel flow model was calibrated using 1.71 m^3/s discharge (Table I). The model was run multiple times and the modelled results were compared to the observed depth-integrated flow velocities, depths and water level values throughout the simulations. For matching the model results with the observations, the Manning's *n*-values were adjusted manually (Table II). The water level was compared at 55 points, depth-integrated velocities were compared at 33 points and water depth was compared at 27 points of the 2013 autumn measurements. The points were selected approximately 20 m apart from each other along the ADCP measurement line. The depth-integrated velocity and depth values were missing from some of the locations, which explain the greater number of points used for the water level calibrations. The MAE (mean absolute error; Equation (1)) was calculated between the model results and observations:

$$\mathrm{MAE} = \frac{1}{N}\sum_{j}^{N}\mathrm{abs}\left(M_j - P_j\right) \quad (1)$$

where N is the number of observations, M_j is the measured value and P_j is the modelled value. Based on the calibration, the *n*-value for river-bed roughness was selected to be 0.04 (Table II). The iterative solver method was applied, as it has worked better than the direct solver in earlier studies (Waddle, 2007). The resulting solution change value, in other words, the difference between the solved parameter values of the last iteration time steps, was also the least with this *n*-value (it should be close to 0.00001). The standard deviation between the velocities, depths and water level of the measurements and the results of the best simulation were 0.11 m/s, 0.09 m and 0.08 m, respectively, at the calibration point locations.

The open-channel flow model was verified in a situation in which the discharge was three times higher (5.10 m^3/s) than in the calibration (Table I). The simulation against this observed higher water level resulted in the following average error values: MAE = 0.03 m, solution change value = 0.00000032. From this time step, there were only water level measurements available. This verified that the model also works at higher discharges and not only at the low pre-winter discharge.

The spatial performance of the model, which applied the final selected *n*-values, was analysed. The mean difference between predicted and observed depths was –0.07 m (see Figure 4). When the absolute difference values were analysed,

Table II. The calibration results of the open-channel flow model, when the pre-winter discharge and water level were applied as the boundary conditions

	Manning's *n*-value	MAE	Solution change value
Flow velocity (m/s)	0.02	0.1157	0.0073497
	0.03	0.1164	0.0058582
	0.04	**0.1160**	**0.0000016**
	0.05	0.1155	0.0093036
	0.06	0.1150	0.0043810
Water level (m)	0.02	0.1120	0.0073497
	0.03	0.1157	0.0058582
	0.04	**0.1190**	**0.0000016**
	0.05	0.1226	0.0093036
	0.06	0.1259	0.0043810
Water depth (m)	0.02	0.0998	0.0073497
	0.03	0.1022	0.0058582
	0.04	**0.1040**	**0.0000016**
	0.05	0.1061	0.0093036
	0.06	0.1084	0.0043810

Note: MAE, mean absolute error. The selected *n*-values for river-bed roughness are bolded.

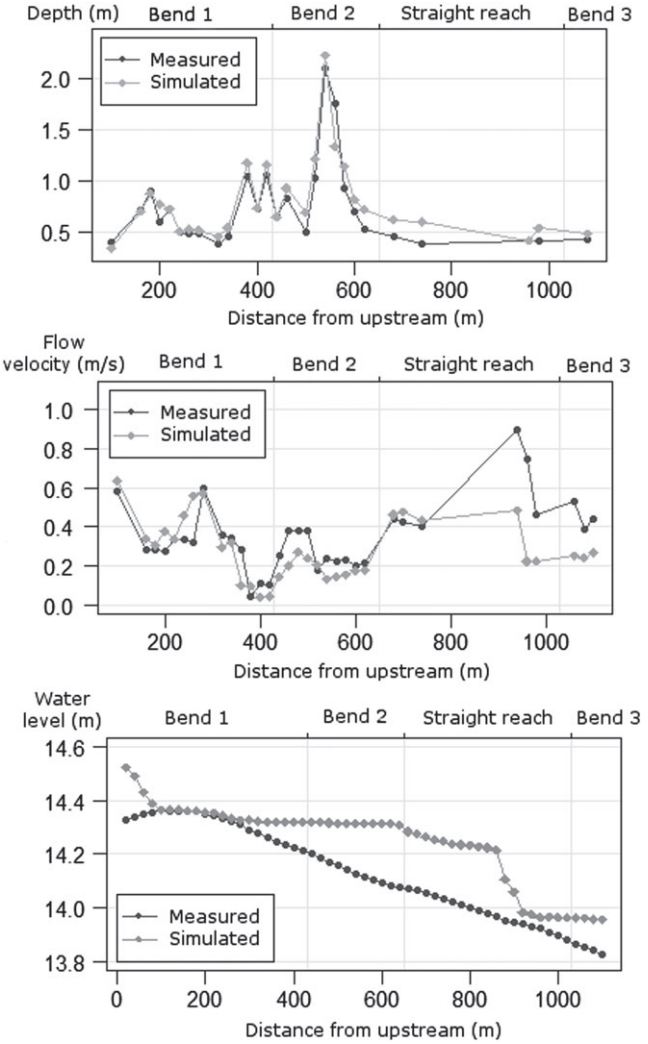

Figure 4. The goodness of the fit between modelled and observed flow velocities, water levels and water depths under open-channel flow conditions.

the average was ±0.10 m. The modelled depth-averaged flow velocities also conformed to depth-averaged flow measurements in the upstream part of the study area (distance: 0–740 m from upstream boundary) where the absolute value of the difference was only ±0.08 m/s. However, the flow velocity model error increased in the downstream section of the study area (see Figure 4; distance: 740–1100 m from upstream boundary). In particular, the error was greatest at the six downstream-most observation points. These differences in the velocities ranged from 0.42 to 0.52 m/s at the downstream part of the straight reach (i.e. the modelled value was 46.3–70.2% less than the measured values) and they ranged from 0.15 to 0.28 m/s in Bend 3 (i.e. the modelled value was 38.6–52.5% less than the measured values).

This could be due to the fact that in autumn 2013 the ADCP measurement was only done longitudinally from the thalweg area, that is to say, in the most probable HVC area, and we did not have measurements from adjacent locations. The explanation for this could be that the modelled HVC did not exactly match these high velocity measurements. Despite this, the HVC was otherwise simulated well in open-channel conditions when compared to the observed HVC locations reported in earlier studies in the same study area (cf. Kasvi *et al.,* 2013b; Lotsari *et al.,* 2017) and prevailing theories (Leopold and Wolman, 1960; Dietrich and Smith, 1983; Engel and Rhoads, 2017). In each of the bends the simulated HVC moved from the inner-bank side of the upstream reach to the outer bank around the apex (see later).

The water level corresponded to observations at the upstream and downstream part of the study area as the absolute values of the observed and modelled differences were 0.05 m within 0–420 m distance from the upstream boundary and 0.08 m within 900–1100 m from the upstream boundary. However, the absolute error for water level had a mean value of 0.2 m in the middle section of the study area (distance: 420–900 m from upstream boundary). All in all, the differences between the results and observations were similar to earlier published studies (Lotsari *et al.,* 2014b). Therefore, the model results can be applied for the analysis of the spatial variation of flow characteristics in the open-channel flow condition.

The calibration of the ice-covered flow model

The ice-covered model simulates, in addition to hydrodynamics, the spatial ISEs, when the thickness and initial downstream ISE are used as inputs for the model. The model understands the ice as a floating ice cover with known ice thickness and roughness, and the ice cover extent is spatially pre-defined (Steffler and Blackburn, 2002).

During the calibration of the ice-covered flow model, the roughness values (Manning's *n*-values) for the ice cover were also defined. Therefore, the model was run multiple times with different ice-cover and river-bed *n*-values (Table III). We applied previous literature as a background for selecting the *n*-values of ice roughness. According to Brunner (2010), the *n*-values of smooth ice are between 0.08 and 0.012. Beltaos (1995) defined that the *n*-value of smooth ice is 0.01. Therefore, we did not test such *n*-values, which would have already been too high or unrealistic based on previous literature and the prevalent, visually interpreted roughness conditions of Pulmanki River. The bed material/bed formations and the ice roughness were similar throughout the study area, based on visual interpretation from drill holes with waterproof cameras,

Table III. The calibration results of the ice-covered flow model

Manning's *n*-value		Velocity (m/s)	ISE (m)	Water depth (m)
Ice cover	River bed	MAE	MAE	MAE
0.005	0.02	0.0308	0.0718	0.0840
0.005	0.03	0.0308	0.0691	0.0838
0.005	0.04	0.0308	0.0676	0.0838
0.005	0.05	0.0308	0.0666	0.0838
0.005	0.06	0.0309	0.0655	0.0838
0.01	0.02	0.0308	0.0683	0.0838
0.01	0.03	0.0309	0.0669	0.0838
0.01	0.04	0.0309	0.0653	0.0838
0.01	0.05	0.0308	0.0640	0.0838
0.01	0.06	0.0308	0.0631	0.0839
0.02	0.02	0.0308	0.0658	0.0838
0.02	0.03	0.0308	0.0641	0.0838
0.02	**0.04**	0.0308	0.0625	0.0839
0.02	0.05	0.0308	0.0618	0.0840
0.02	0.06	0.0308	0.0601	0.0841
0.03	0.02	0.0308	0.0645	0.0838
0.03	0.03	0.0308	0.0626	0.0840
0.03	0.04	0.0308	0.0605	0.0841
0.03	0.05	0.0307	0.0590	0.0842
0.03	0.06	0.0307	0.0579	0.0843

Note: ISE, ice surface elevation; MAE, mean absolute error. The bolded values are the Manning's *n*-values selected for the ice-covered flow model.

Table IV. The absolute values of the average differences between the observed and simulated parameters in winter 2014

	Depth (m)	Velocity (m/s)	ISE (m)	IWIE (m)
Bend 1 (cs 7)	0.07	0.03	0.07	0.07
Bend 2 (cs 3)	0.07	0.02	0.06	0.06
Bend 3 (cs 3)	0.11	0.04	0.05	0.05
All cross-sections (n = 12)	0.09	0.03	0.07	0.05

Note: One cross-section was selected from each bend, and also the middle channel longitudinal profile was analysed from all 12 cross-sections. The simulated values were subtracted from the observed ones, absolute values were defined and then the averages were calculated. ISE, ice surface elevation; IWIE, ice–water interface elevation.

and therefore a uniform n-value was the best solution for our model.

The resulting simulated depth-integrated velocities, ISEs and water depths were compared to the ones measured in 46 locations. These locations were taken from the cross-section of each bend, which had the greatest number of drill holes (i.e. measurement locations). In addition, the mid-measurement location of each cross-section was included in the calibration.

The n-values had hardly any effect on the depth-integrated flow velocities (Table III). However, the errors (MAEs) for the ISEs were the smallest when the ice-cover and river-bed n-values were the greatest. The errors in water depth did not have clear dependence on n-values. So, when both the ice-cover and river-bed n-values were around the mean of all the tested values, all the simulated parameter values corresponded best to the observations. Based on this, a river ice-cover n-value of 0.02 was selected, which coincides with the generally suggested roughness value for rippled ice (Brunner, 2010). The river-bed n-value was selected to be 0.04, which is the same as for the open-water simulations.

The spatial performance of the ice-covered model, which applied the final n-values that were selected, was analysed. The simulation results matched the observations in different bends (Tables IV and V). It is noteworthy that the modelled velocities were underestimated by the model in the measured high-velocity locations of the cross-sections at Bends 1 and 3 (Figure 5). The maximum underestimations were 0.06 m/s (Bend 1) and 0.10 m/s (Bend 3). The model also followed the overall velocities well in Bend 2, but smoothed the variation of velocities between adjacent measurement verticals. Along the middle channel longitudinal profile of the study area, velocities followed the observations well (Table IV, Figure 5). The modelled HVC moved from the inner-bank side of the upstream part of the bend to the outer-bank side around the apex in each of the bends. This model result was similar to the modelled and measured open-channel flow's HVC movement. However, the highest measured ice-covered velocities were located slightly more towards the inner or outer bank than the simulated HVC, particularly in the downstream part of Bends 1 and 3, and also upstream of the apex of Bend 1 (see later). Despite these discrepancies, the broadscale locations of the simulated ice-covered HVC resembled the measurements (see also Lotsari *et al.*, 2017).

Both ISE and IWIE values were very close to the measured ones, with a slight underestimation (Table IV, Figure 6). It is noteworthy that the modelled ISE did not vary as much along

Table V. The standard deviations (SDs) of the differences between winter simulation results (i.e. the best final simulation) and the observations at the calibration locations

	Bend 1 (cs7)	Bend 2 (cs 3)	Bend 3 (cs3)	Middle points of all cross-sections
SD of depth comparison	0.06	0.06	0.07	0.06
SD of velocity comparison	0.02	0.01	0.03	0.02
SD of ice surface elevation comparison	0.02	0.02	0.02	0.04

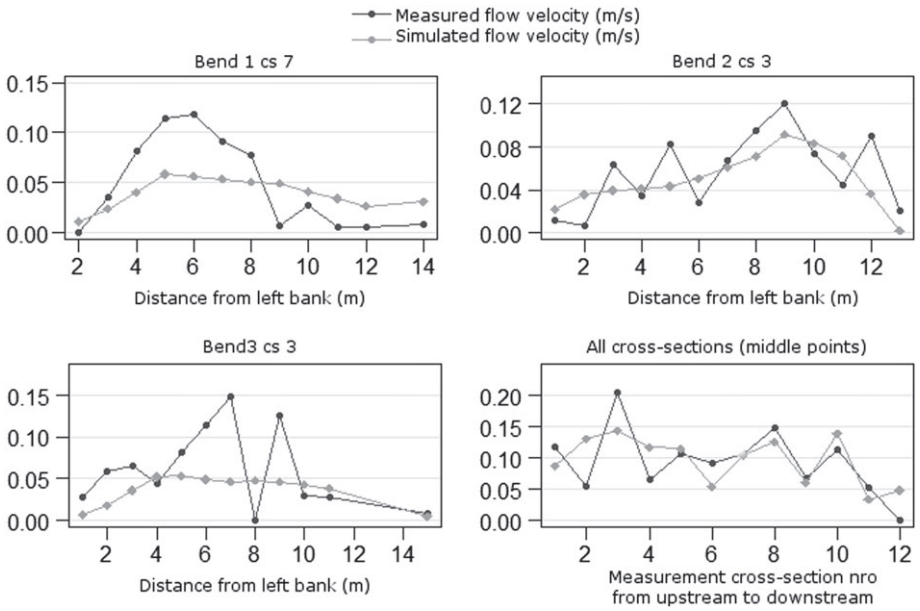

Figure 5. The goodness of the fit between modelled and observed depth-averaged flow velocities in ice-covered river.

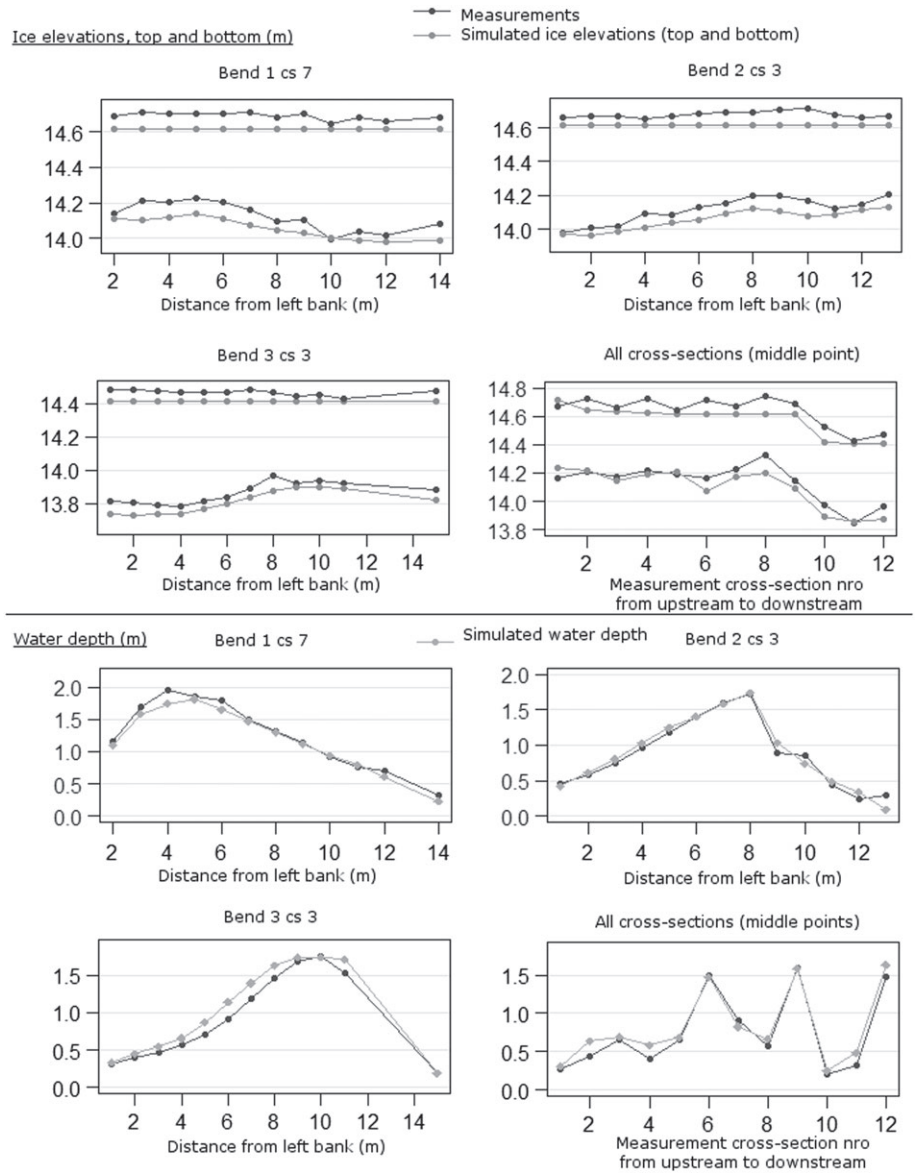

Figure 6. The goodness of the fit between modelled and observed ice-covered water depths, and the elevations of ice surface and ice–water interface.

the cross-sections as was observed (i.e. the modelled ice surface was flatter than observed). However, when observing the longitudinal ice surface profile, that is, the centre points of each of the cross-section, the ISE corresponded to the observations. The simulated depths and ice thicknesses were also similar to the cross-sectional observations (Table IV, Figure 6), in other words, the ice was thicker on the inner-bank side and thinner on the outer-bank side of the bends. Therefore, the ice-covered model results were considered suitable for analysing the spatial variation of the depth-averaged flow velocity, horizontal flow directions, shear velocity, and the erosion and sedimentation potential.

Note that River2D does not calculate bed shear stress, only shear velocity, which characterizes the shear at all boundaries. It is typically expressed as $V^* = \mathrm{sqrt}(\tau/\rho)$, where τ is the bed shear stress and ρ is the fluid density (Steffler and Blackburn, 2002; Simões, 2014). Thus, in the open-channel model, the shear velocity could be used to calculate the bed shear stress using the equation. However, if calculating τ from the shear velocity of the ice-covered model, the resultant τ represents the average shear stress (i.e. the average of both the bed and ice shear stresses). Therefore, we did not post-process the model outputs to calculate the shear stress as such results would have been non-comparable between seasons.

Erosion–sedimentation potential calculations

Thus, due to model output limitations, the only parameter received from the model which was possible to compare in the final analyses between the seasons regarding the incipient motion of sediment particles was that of the depth-averaged velocities. For justifying the application of the depth-averaged velocities for erosion–sedimentation potential analyses, as many critical velocity calculation methods apply near-bed velocities, we calculated the difference between the measured depth-averaged and near-bed layer velocities. The difference between the autumn 2013 near-bed and depth-averaged velocity was on average –0.01 m/s, meaning that the near-bed layer velocity was greater than the depth-averaged velocity. The standard deviation was 0.09 m/s. The difference between winter 2014 near-bed and depth-averaged velocity was on average –0.01 m/s, and its standard deviation was 0.10 m/s. Thus, the near-bed layer velocity was again greater than the depth-averaged velocity, and this difference was greater than in the autumn. Note that the ADCP leaves a section of water at the bottom unmeasured (Sontek, 2018), and the near-bed layer velocity means that the velocity was measured *c.* 4-17 cm above the river bed, depending on the measurement vertical. Thus, we find the application of

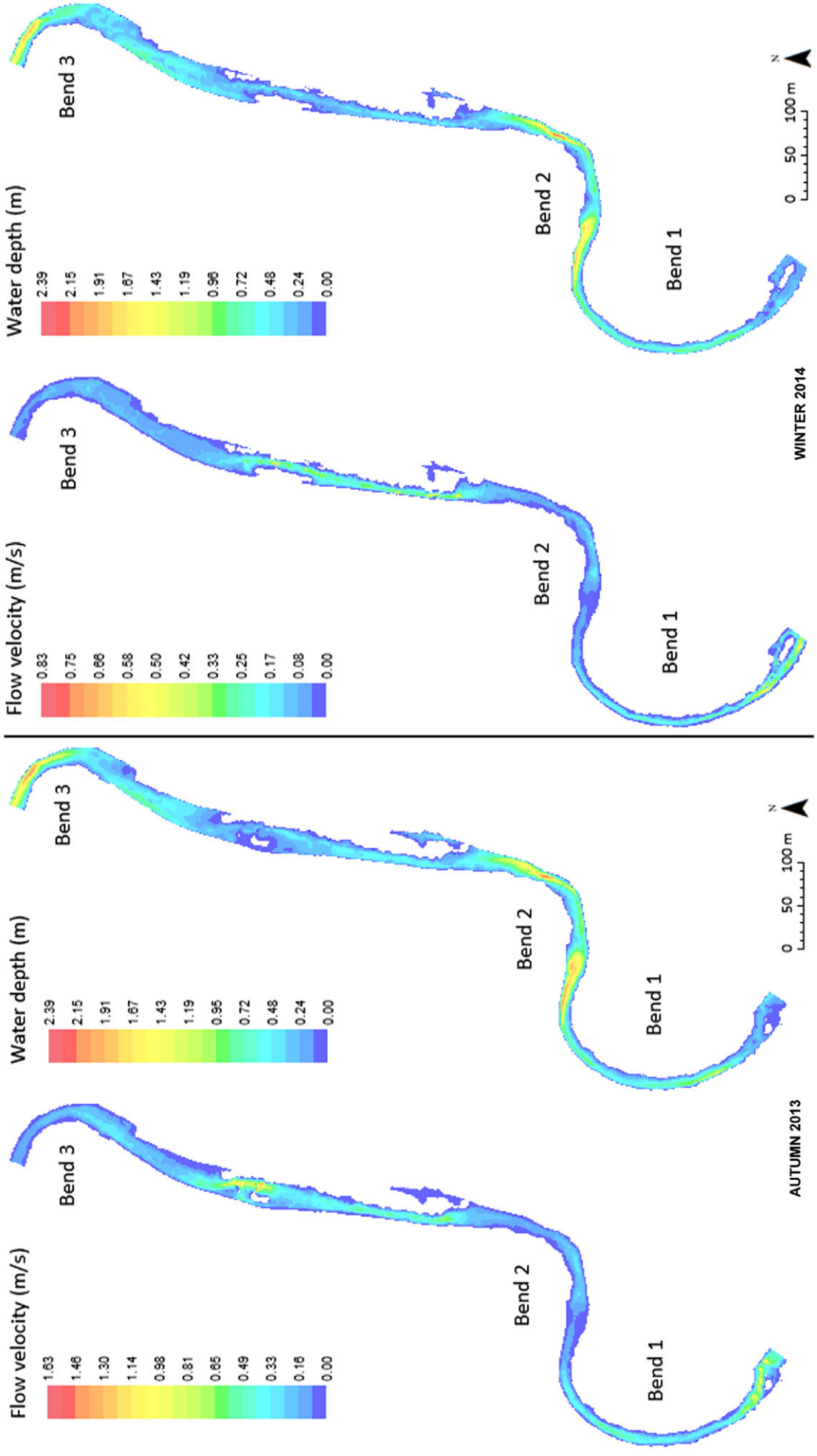

Figure 7. The depth-averaged flow velocity and depth distribution based on open-channel flow model of autumn 2013 and ice-covered flow model of winter 2014. [Colour figure can be viewed at wileyonlinelibrary.com]

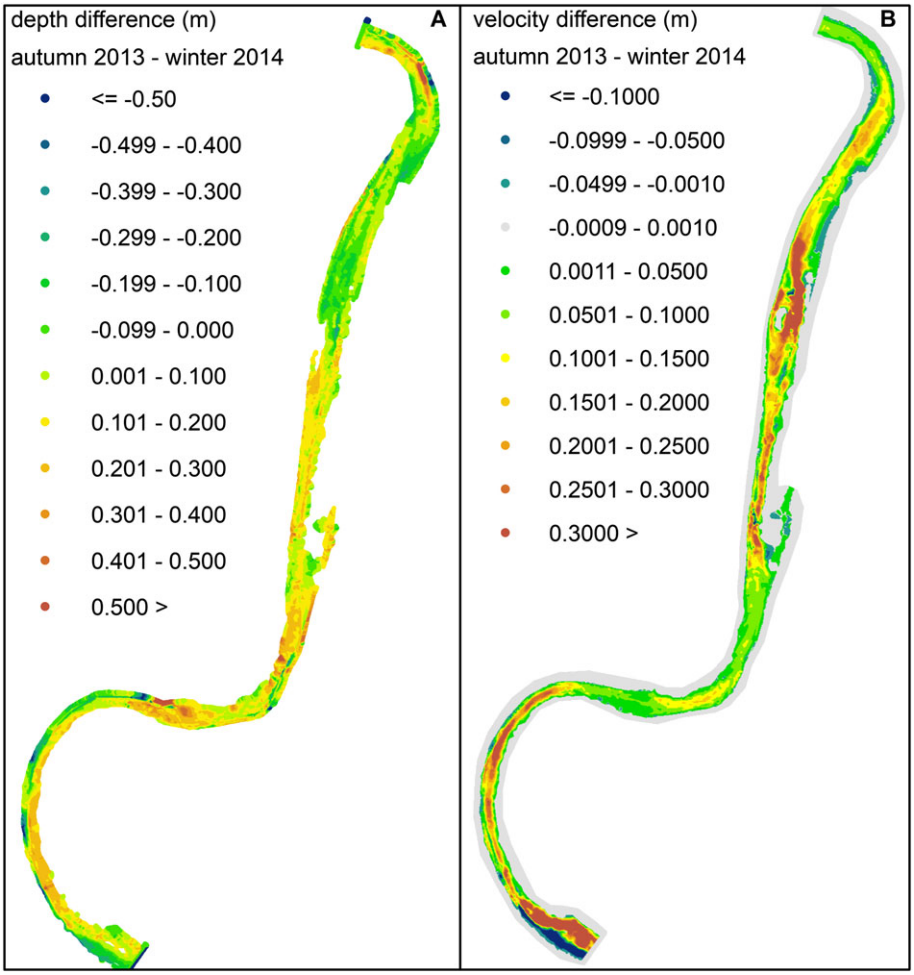

Figure 8. The difference of autumn 2013 and winter 2014 (A) depth and (B) velocity. The positive values indicate that the depth and velocities have been greater in the autumn than in the winter. [Colour figure can be viewed at wileyonlinelibrary.com]

the depth-averaged velocity justifiable as the point of the article was to show the relative differences between the seasons.

The critical velocities required for moving the channel sediment were calculated, and then their exceedance was compared to modelled and measured velocities. For this purpose, channel bed sediments were sampled using a grab sampler in the 2013 autumn low flow period. The D_{50} values were calculated for the 22 sample locations, which were under water during the simulated winter and autumn situations. The critical velocity thresholds for incipient motion were defined for these sediment samples based on the Hjulström (1935) diagram. The minimum, average and maximum critical velocities of these 22 analysed samples were also defined. The Hjulström diagram was selected due to its wide usability and simplicity. However, we acknowledge the limitations if the approach of Hjulström (1935) is only applied for the depth-averaged velocities as it has been created based on near-bed velocities. Therefore, in addition to the modelled depth-averaged velocities, we compared the measured depth-averaged and near-bed velocities to the calculated critical thresholds.

Firstly, the exceedance of the minimum, maximum and average critical velocities were investigated using both the near-bed and depth-averaged flow velocities measured with the ADCP in autumn 2013 and winter 2014. Secondly, the simulated autumn 2013 and winter 2014 depth-averaged velocities were compared against these minimum, maximum and average thresholds throughout the channel. Thirdly, the actual critical thresholds of each sediment sample were compared to the modelled ice-covered and open-channel velocities at the sediment sample locations in order to analyse the differences in the erosional conditions between seasons. Therefore, we can bring together the relative differences in the erosion–sedimentation potential between the seasons, which is the main purpose of the article.

Results

Spatial variation of the simulated open-channel and ice-covered flow characteristics

Overall, during open-channel conditions the water depths of each bend were deepest in the downstream part and on the outer-bank side of each meander bend, and the shallow water areas were dominantly located in the upstream part of each bend (Figure 7). The straight reach between Bends 2 and 3 was also shallow (i.e. the water depth was less than 0.5 m; Figure 7). Despite the ice-covered discharge (0.63 m^3/s) being smaller than in the preceding autumn open-channel conditions (1.71 m^3/s), the maximum depths were similar, even though the bathymetry had been modified to include the winter 2014 bed elevations from the cross-sections. For the ice-covered model the deepest and shallowest simulated areas in winter 2014 were almost in the same locations as in autumn 2013 (Figures 7 and 8). The shallowest flow was in the straight reach and in the upstream part of Bend 1. The deepest area was on the outer-bank side of each meander bend. However, differences also occurred between winter and autumn. The overall depths were shallower in winter than in autumn (Figures 7 and 8). The river was also narrower in the winter due to the ice cover. Although the ice cover was not attached to the banks in the outer parts of

the bends, the areas, which were shallow in the autumn, had been frozen to the river bed based on observations.

A deep pool area with slow flow velocities of < 0.16 m/s characterized the reach between Bends 1 and 2 in autumn 2013 (Figures 7 and 8). In winter, the values were < 0.08 m/s in this pool area. The highest simulated open-channel flow velocities were in the middle of the straight reach and in the upstream part of Bend 1, where the water depths were the shallowest in autumn 2013. The flow velocities exceeded 0.65 m/s in these locations. In addition, the autumn flow velocities were high around the apex and at the upstream parts of the bends. Cross-sectionally, the open-channel flow velocities were generally greater along the outer bank of the bend than on the inner-bank side. An exception is the upstream part of the bends, where the situation was the opposite. The simulated HVC of the open-channel flow moved in all three bends from the inner bank to the outer bank, when moving from upstream to downstream within each bend.

The modelled ice-covered flow velocities were smaller than in the open-channel conditions, 73% of the area being less than 0.1 m/s, but greater than 0 m/s. The comparative value was 35% in open-channel conditions. The maximum velocity in autumn (1.51 m/s) was double the maximum velocity of winter (0.77 m/s). Similar to the autumn 2013 simulations, the ice-covered velocities were greatest in the shallowest areas and smallest in the deepest locations. Overall, the ice-covered flow velocities were greater closer to the outer bank compared to the inner bank around the apexes of each bend. In Bend 1, the simulated ice-covered velocities were greatest in the upstream part and slowest in the downstream part. In winter, there was not such a clear high velocity and shallow depth location around the apex as there was in the autumn. In Bend 2, the greatest ice-covered velocities were upstream of the apex area. Velocities were also high downstream of Bend 2 (i.e. where the straight reach began). In Bend 3, the winter velocities were greatest in the upstream part and middle part of the bend, whereas in the downstream part the velocities were smallest. Thus, also in winter, the simulated HVC moved from the inner bank along the upstream part of the bend to the outer bank around the apex in each of the bends.

The clearest differences between the seasons were in the formation of the horizontal RFSs (Figures 9 and 10). The low flow velocities occurred in the middle of these RFSs. In open-channel conditions, the clearest and greatest RFS occurred in the downstream part of Bend 1 (Figure 9b). This large clockwise recirculating pattern occurred on the inner-bank side, and on the outer-bank side, the flow was diverted towards the bank, even though no recirculating patterns of flow occurred there. This large clockwise RFS was located in the area of the highest curvature of the bend. The flow velocities were slow (< 0.10 m/

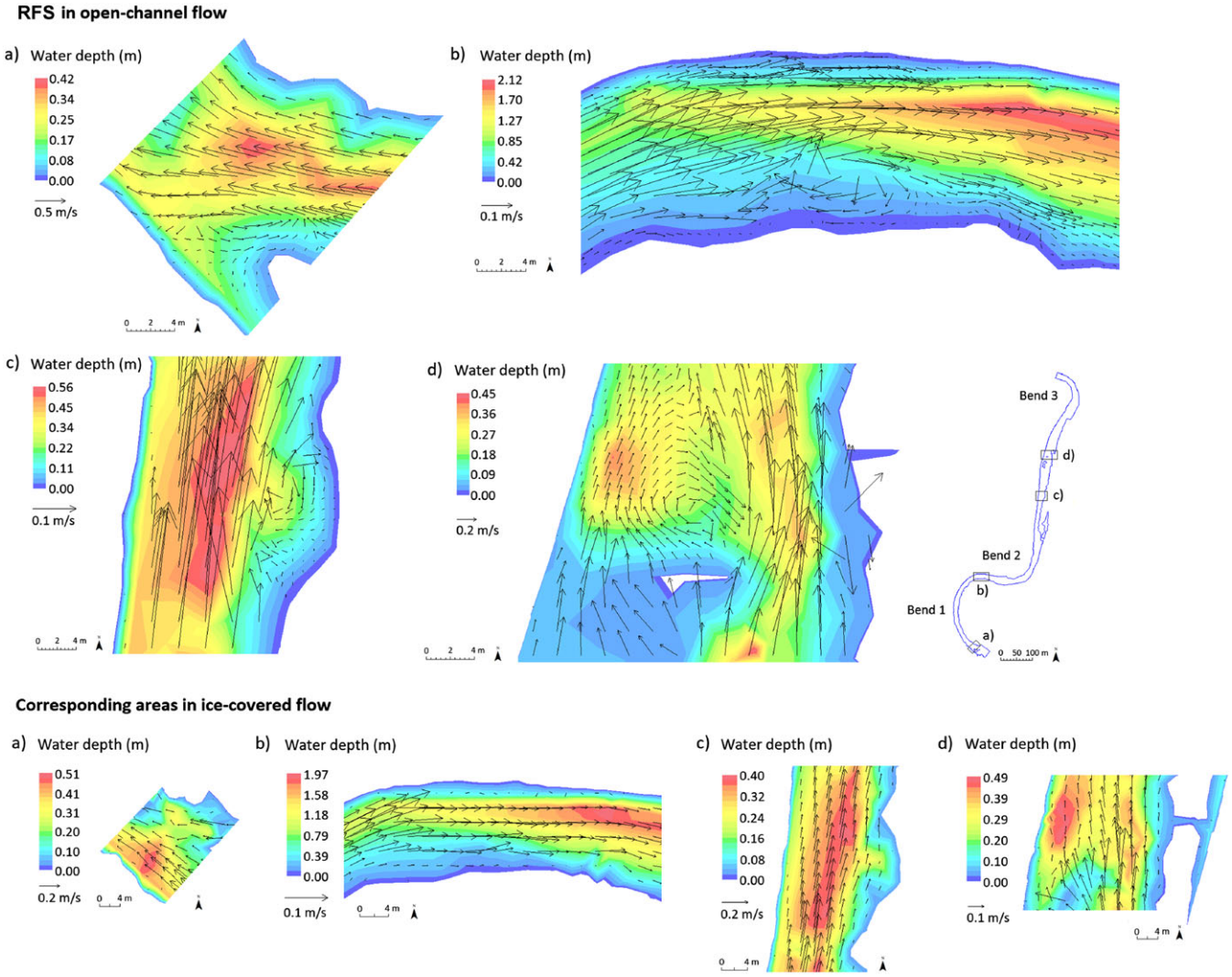

Figure 9. The recirculating flow structures (RFSs) formed in an open-channel flow model and the corresponding locations in an ice-covered situation. The greatest RFSs were in Bend 1 in autumn (b). [Colour figure can be viewed at wileyonlinelibrary.com]

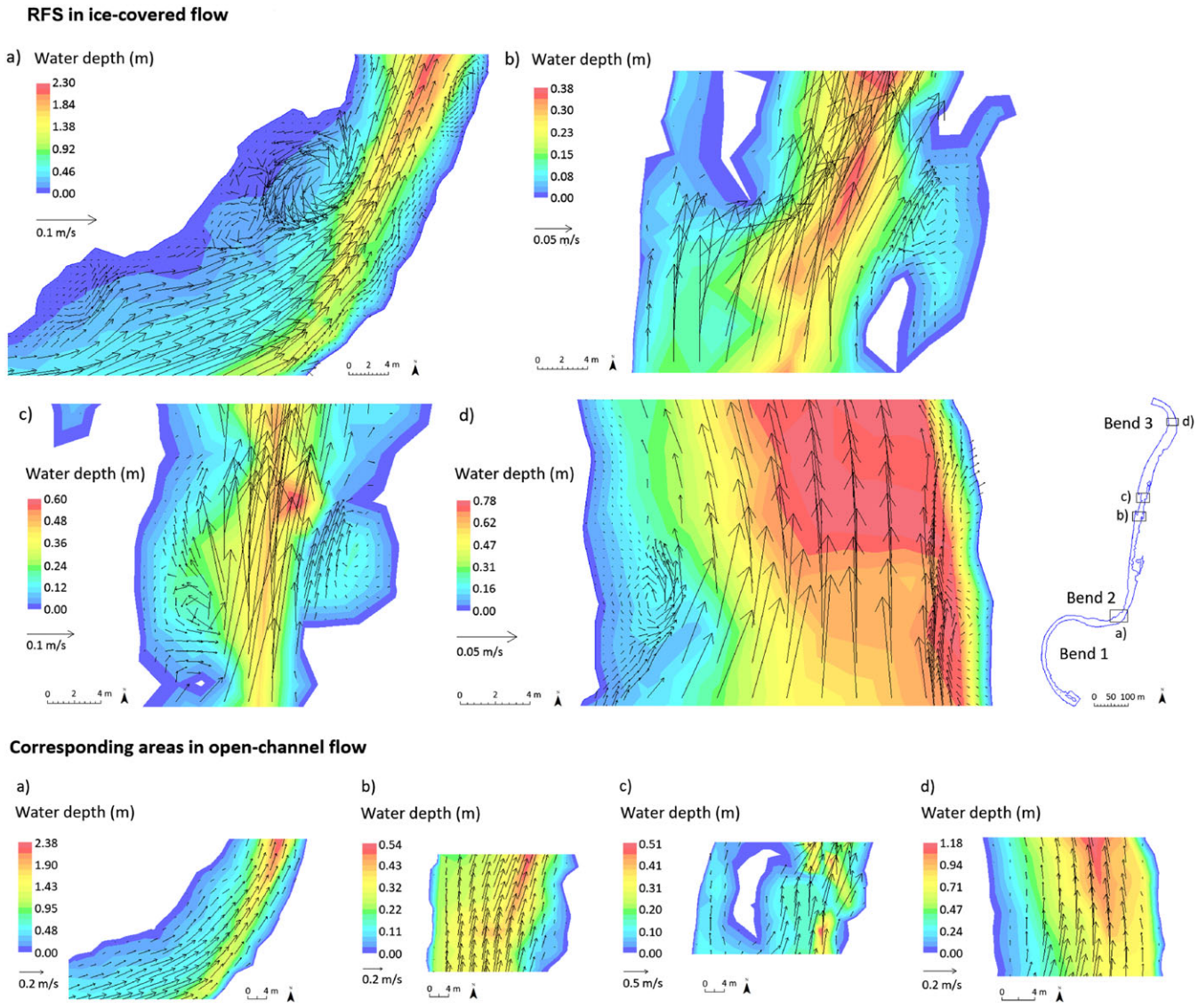

Figure 10. The recirculating flow structures (RFSs) formed in the ice-covered flow model and corresponding locations in an open-channel situation. The greatest RFSs were in Bend 2 in winter (a). [Colour figure can be viewed at wileyonlinelibrary.com]

s) around this RFS and downstream of it, but higher (0.10–0.30 m/s) upstream of this flow structure and on the outer bank side. The shallow flow depths on the inner-bank side at the location of the RFS presumably enhanced the formation of this flow structure. In addition, some smaller RFSs were observable in the upstream part of Bend 1 (Figure 9a) and downstream of the mid-channel bars of the straight reach in autumn (Figure 9d). These smaller flow patterns were caused by obstacles within the channel area and were not due to the forces related to the curvature of the channel. In addition, there was a RFS in the straight reach, in the location where the narrow channel widens in open-channel conditions (Figure 9c). Around it, the simulated flow was directed towards the banks.

In Bend 2, a large anti-clockwise RFS formed at the inner bank around the apex area in winter (Figure 10a). There were two smaller RFSs next to this large RFS, on its upstream (anti-clockwise) and inner-bank (clockwise) sides. Also, there were weaker RFSs further upstream on the inner-bank side and at the downstream part of the bend on the outer-bank side. Thus, there was a group of these RFSs in Bend 2. During both open-channel and ice-covered conditions, the flow depths were shallow in the upstream part of the RFSs (on the RFS of Bend 1 in autumn and on the RFS group of Bend 2 in winter) and there was deep water on the downstream side of the RFSs. In addition, in Bend 3, there was a small anti-clockwise circulation of flow in the upstream section along the inner bank in winter (Figure 10d). Downstream of this RFS, the flow was directed towards the bank. Also, RFSs were formed in the straight reach between Bends 2 and 3 in ice-covered conditions (Figures 10b and 10c). These were located where the channel suddenly widened towards downstream. Overall, there was more spatial variation in the flow direction next to the banks in winter than there was in autumn. However, the flow was not systematically directed either towards the inner or outer banks under ice cover.

The erosion potential during open-channel and ice-covered low flow conditions

The maximum shear velocity was 0.199 m/s in the open-channel conditions, but the maximum shear velocity was smaller under ice cover, being 0.121 m/s (Figure 11). In winter, the shear velocity was mostly below 0.015 m/s, as only 17% of the flow area had values higher than 0.015 m/s. On the contrary, in autumn wide areas of above 0.015 m/s shear velocity existed (45% of the flow area). The spatial distribution of the shear velocity was narrower in the winter, thus making the autumn high shear velocities spread more widely within the

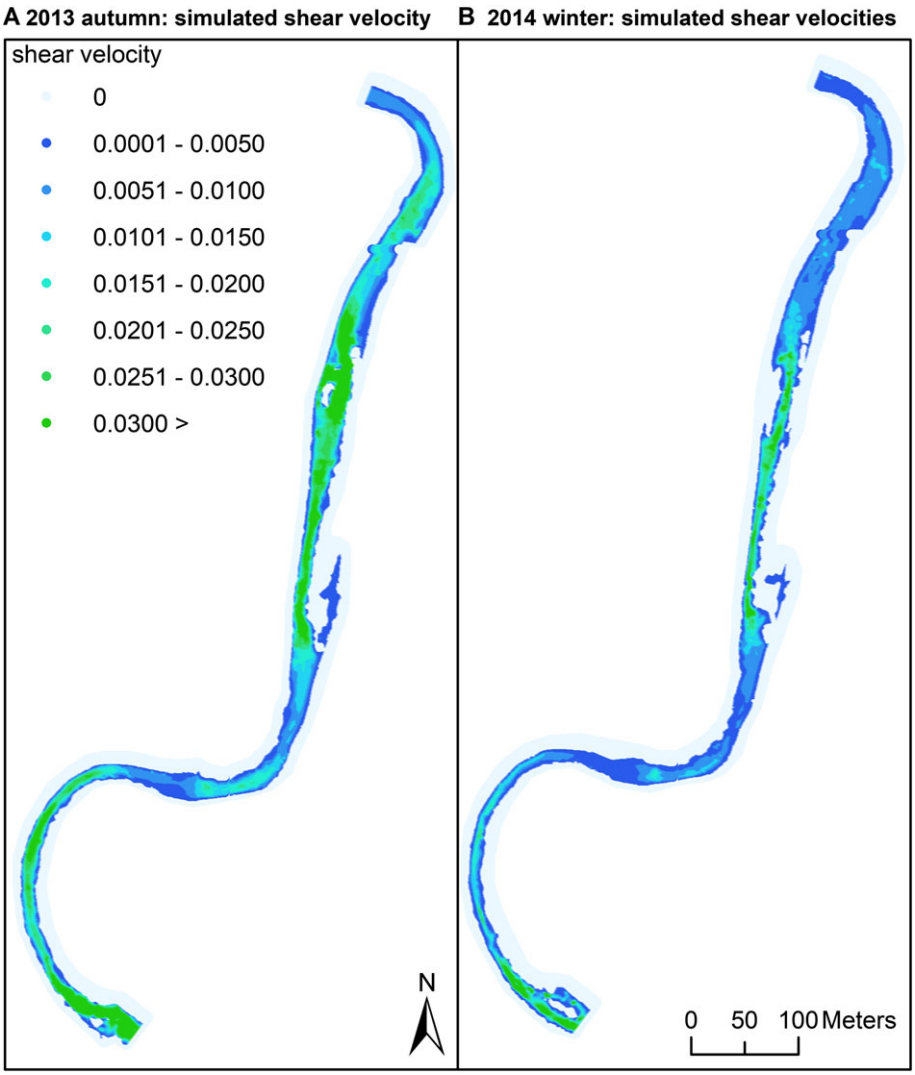

Figure 11. The shear velocities (m/s) of simulated open-channel and ice-covered flow. [Colour figure can be viewed at wileyonlinelibrary.com]

channel. Similar to the case of simulated depth-averaged velocities, the straight reach and the upstream section of Bend 1 experienced the highest shear velocities, both in open-channel and ice-covered conditions. The least prone areas for high shear velocities were in the pool area between Bends 1 and 2 and in the downstream sections of Bends 2 and 3 during both seasons.

For quantifying the erosion-sedimentation potential, locations where the near-bed and depth-averaged velocities exceeded the critical thresholds for particle movement were defined. The velocities throughout the whole study area were compared to the minimum critical velocity threshold (0.23 m/s), mean critical velocity threshold (0.30 m/s) and maximum critical velocity threshold (0.72 m/s) for incipient movement calculated based on the D_{50} sediment particle sizes of the 22 sediment samples (Table VI, Figures 1, 12, and 13). These critical velocities corresponded to the sediment D_{50} values of 0.303, 0.700 and 3.625 mm for the minimum, mean and maximum critical velocity threshold, respectively.

The ice-covered near-bed velocities of the ADCP measurements exceeded the minimum threshold for particle movement (at 10% of the observation points) more often than the depth-averaged velocities did (at 7% of the observation points) (Figures 12 and 13). The near-bed velocities were exceeded, especially in the upstream parts of Bends 1 and 3, and in the apexes of all bends in winter 2014 (Figure 12). When the depth-averaged ice-covered flow velocities, which had been measured in cross-sections, were compared to the minimum critical velocity threshold, the threshold value was exceeded in the upstream sections and the apexes of Bends 1 and 3. The ADCP measurements of Bend 2 did not have depth-averaged velocities which exceeded the minimum critical velocity for particle movement in ice-covered conditions (Figure 13). Note that in the locations where measured depth-averaged velocities exceeded the critical thresholds, the near-bed layer velocities also exceeded them (Figures 12 and 13).

The measured depth-averaged flow velocities of the open-channel conditions (autumn 2013) exceeded the minimum critical velocity threshold in most (i.e. 61%) of the flow velocity measurement locations (Figure 13). However, also 61% of the near-bed velocity measurement points exceeded the minimum critical threshold (Figure 12). Note, that these measurements had been taken along the longitudinal profile, that is, along the thalweg. In autumn 2013, the near-bed layer velocities also exceeded the thresholds in the straight reach. Furthermore, the autumn near-bed layer velocities exceeded the minimum, maximum and average thresholds more often than in the winter 2014.

The simulated depth-averaged velocities were greater than the average critical velocity threshold in the upstream part of Bend 1, as well as in the straight reach, during ice-covered flow conditions (Figure 13). The average critical velocity threshold

Table VI. The D_{50} sediment particle sizes, their critical velocity thresholds for movement (Hjulström, 1935), and the simulated winter and autumn velocities in these measurement locations

Point	D_{50} (mm)	Critical velocity for D_{50} (m/s)	Velocity (winter) (m/s)	Velocity (autumn) (m/s)
P1	0.828	0.34	0.00	0.05
P3	0.554	0.28	0.00	0.04
P5	0.730	0.32	0.10	0.28
P7	0.578	0.28	0.01	***0.31***
P9	0.350	0.23	0.06	0.29
P11	0.454	0.25	0.18	0.33
P13	0.466	0.25	0.16	***0.43***
P15	0.501	0.27	0.00	***0.32***
P17	0.728	0.31	0.23	***0.35***
P19	0.975	0.35	0.22	***0.54***
P21	0.630	0.29	0.18	***0.31***
P23	3.625	0.72	0.10	0.22
P25	0.483	0.26	0.00	0.01
P27	0.384	0.24	0.00	0.01
P29	0.467	0.25	0.00	0.03
P31	0.303	0.23	0.14	0.20
P33	0.458	0.25	0.11	0.20
P35	0.475	0.26	***0.40***	***0.36***
P37	0.409	0.24	0.18	***0.38***
P39	1.060	0.36	0.26	***1.07***
P41	0.550	0.28	0.09	0.21
P43	0.581	0.28	0.01	0.06

Note: The values shown in bold and italic typefaces are the ones which exceed the critical threshold.

was exceeded in simulated open-channel conditions in the upstream and apex area of Bend 1, in the straight reach and in the upstream part of Bend 3. For both the open-channel and ice-covered model results, the minimum critical velocity threshold was exceeded in the apex area of Bend 1 and also in the straight reach. In addition, the open-channel velocities exceeded this minimum threshold around the apex of Bend 2. The maximum critical velocity threshold was exceeded in the case of simulated ice-covered flow conditions for only two locations in the straight reach (Figure 13). In simulated open-channel conditions, this velocity of 0.72 m/s was exceeded within small areas of the upstream part of Bend 1 and in the straight reach.

When the actual critical velocity thresholds of each of the 22 sediment samples were compared at their measurement location to the simulated depth-averaged flow velocities, the critical threshold was exceeded in nine locations during the open-channel flow conditions and in one location during ice-covered flow conditions (Figure 1). This one location where the simulated velocities exceeded the threshold in both seasons (sample P35), was in the straight reach downstream of Bend 2. Simulated open-channel velocities also exceeded critical thresholds in two other sediment sample locations in the straight reach (P37 and P39, Table VI and Figure 1). The rest of the sediment samples whose critical velocity thresholds were exceeded in open-channel conditions were located in the apex area of Bend 1.

The exceedance of critical velocities at the sediment sample locations (Figure 1) and the exceedance of the overall minimum critical velocity (Figure 13) when the thresholds were compared to the simulated depth-averaged velocities are consistent with each other. In addition, the locations where the minimum critical velocity was exceeded based on the depth averaged and near-bed layer ADCP velocity measurements (Figure 12) were in line with these simulated velocities. Therefore, it was possible to gain the seasonal variability in the locations of the most potential erosion and deposition based on the results.

Discussion

Model performance

The sensitivity analyses during the model calibration showed that it was suitable for simulating spatially varying flow characteristics during open-channel and ice-covered seasons. Overall the modelled depth, water/ice elevations, ice-cover thicknesses and depth-averaged velocities corresponded to the observations. Similar to the simulations of the present study, ice cover has earlier been observed to be thickest along the inner bank of the bends (Sui *et al.,* 2008; Wang *et al.,* 2011; Kämäri *et al.,* 2017). The modelled ISEs and IWIEs were only 0.01–0.13 m lower than the observed values (cf. Figure 6). However, these small differences might have potentially affected the simulated flow velocities, as the ice-covered model underestimated the cross-sectional peak flow velocities. The model smoothed the cross-sectional variability of velocities between adjacent measurement verticals when compared to the measurements. The open-channel flow model underestimated the flow velocities in the downstream part of the straight reach and in Bend 3, most probably due to the differences in the measured and simulated HVC location (see Data and Methods section). Despite this underestimation, these simulated velocities exceeded the critical minimum velocities for particle motion. Thus, these underestimations did not impact on the erosion potential analyses.

In the River2D model, even though the user predefines the observed ice elevation in the model as an initial downstream boundary value, this ice elevation is not fixed throughout the simulations (Steffler and Blackburn, 2002). This means that the model assumes the ice cover to be floating, and the model computes the ice elevation based on the initial ice elevation boundary value and roughness values fed by the user. If the location of the ice elevation had been at the initial elevation throughout the simulations with River2D, the model could have possibly been able to simulate higher peak flow velocities than it did. During winter, pressurized conditions of flow could take place when the cracks in the ice cover freeze for short periods of time (Turcotte *et al.,* 2011). The impact of possibly increased velocities and related erosion during these short-lived pressurized conditions could be important for the channel morphology (Turcotte *et al.,* 2011). Ettema (2002) has also stated that the flow concentrates in the thalweg when the river ice cover is attached to the banks. As said, in addition to the open water locations in the two upstream measurement cross-sections of March 2014, the ice cover was not attached to the banks on the outer banks of bends. Therefore, the floating ice cover conditions occurred in March 2013, and the selection of River2D for ice-covered flow simulations was justifiable. However, further tests with different models, and particularly with models created for pressurized flow, would be the next step to apply in the study area. Also, it would be preferable to calibrate these different models with data from multiple years and ice-cover conditions.

The depth-averaged velocities, which were the only comparable simulated parameter between the seasons, were applied for the final analyses of spatial flow structures and erosion–sedimentation potential. River2D does not calculate the separate bed and ice shear stresses under ice cover (Steffler and Blackburn, 2002). As the aim of the article was to show the relative differences between the seasons, we find the application of the depth-averaged velocity justifiable for our purposes.

The Hjulström (1935) diagram was selected due to its simplicity and wide usability, and model output and field data limitations. The Shields criterion (Shields, 1936; Lamb *et al.,* 2008) and movability numbers (Khelifa and Hill, 2006; Simões,

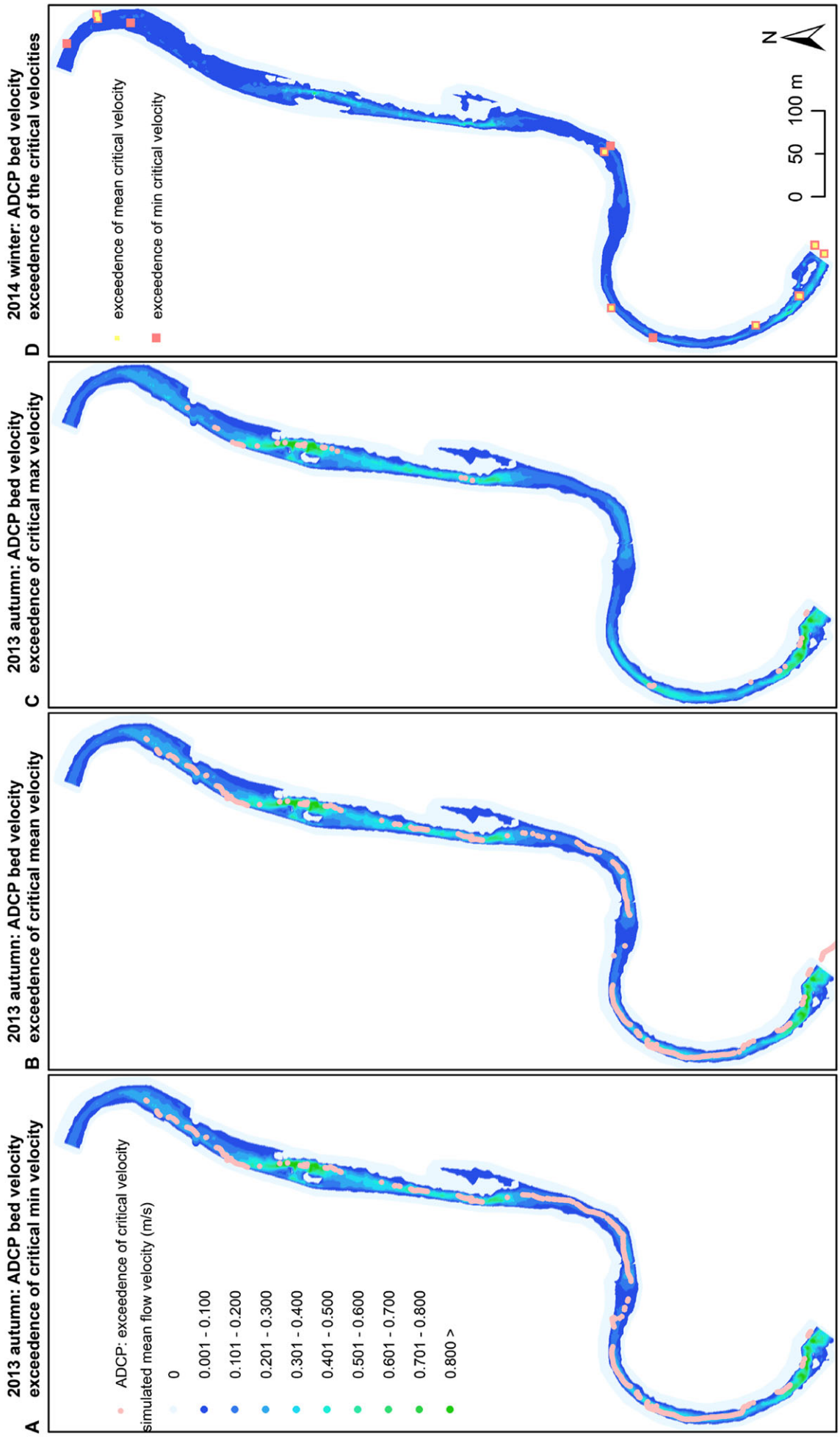

Figure 12. The exceedance of the minimum and average critical velocity thresholds by the measured [with Acoustic Doppler Current Profiler (ADCP)] near-bed velocity on 3 March 2014. The simulated velocities of winter 2014 are on the background. Thus, the bed velocities were exceeded more often than the depth-averaged velocities based on the ADCP analysis. [Colour figure can be viewed at wileyonlinelibrary.com]

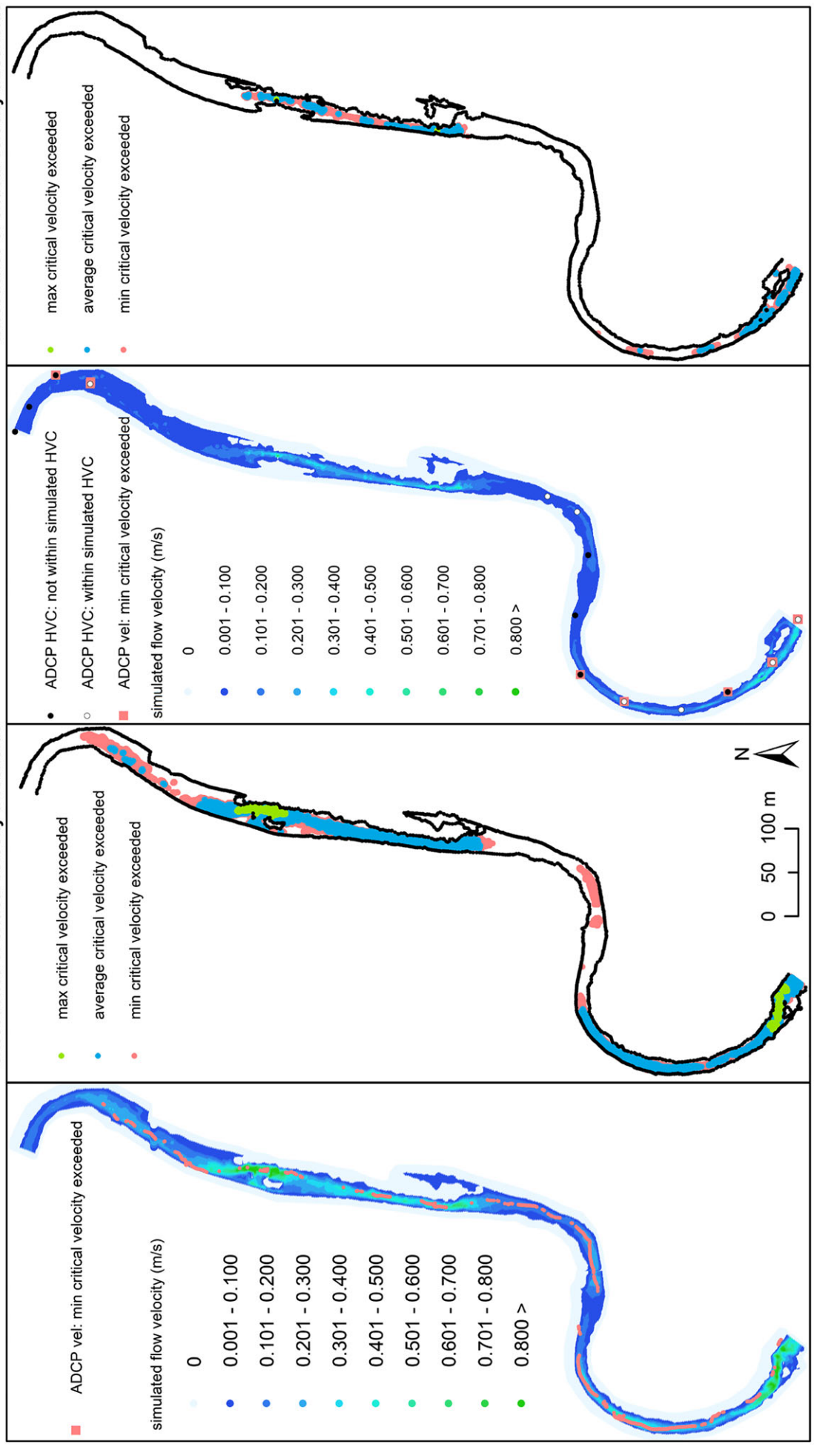

Figure 13. (A) The high velocity core (HVC) (depth-averaged flow) of autumn 2013 simulation. The exceedance of the minimum critical velocity for sediment particle movement is also shown based on depth-averaged [acoustic Doppler current profiler (ADCP)] flow measurements. (B) The locations where the simulated depth-averaged open-channel flow velocities exceed the minimum, average and maximum critical velocities for particle movement. (C) The HVC (depth-averaged flow) of winter 2014 simulation, and based on depth-averaged flow measurements (ADCP). The velocity measurement verticals of each cross-section, which had the greatest velocity, are shown. The locations of the measured HVC are depicted in comparison to the simulated HVC locations. The exceedance of the minimum critical velocity for particle movement is also shown. (D) The locations where the simulated ice-covered depth-averaged flow exceeded the minimum, average and maximum critical velocities for sediment particle movement. [Colour figure can be viewed at wileyonlinelibrary.com]

2014), which apply for example settling velocity equations, bed shear stresses and sediment densities for their derivation, were discarded, because theoretical parameter values would have been needed to apply for the calculation. Thus, these equations would not have resulted in any more confident results than those gained from the Hjulström (1935) method. We acknowledge the limitations if the approach of Hjulström (1935) is only applied for the depth-averaged velocities. The comparison between our measured (with the ADCP) near-bed and depth-averaged velocities confirms that where the depth-averaged velocities exceeded the threshold for particle movement, the near-bed layer velocities also exceeded the threshold values.

The spatial distribution of the seasonal flow velocities

The modelled open-channel HVC locations resembled the results of previous measurement-based studies performed in the same study site (Kasvi *et al.,* 2013b; Lotsari *et al.,* 2017). This followed the well-established theories that the HVC moves from the inner-bank side of the upstream section towards the outer bank at the downstream section of the bend (Leopold and Wolman, 1960; Dietrich and Smith, 1983; Engel and Rhoads, 2017). The modelled HVC locations in the ice-covered flow conditions had similarities to the study of Wang *et al.,* (2010) who had showed that in ice-covered conditions the HVC also moves from one bank to another in a meandering channel. Lotsari *et al*. (2017) also found the broadscale movement of the HVC from one bank to another, based on cross-sectional measurements; however, at a more detailed scale the HVC varied more between consecutive cross-sections in ice-covered conditions than during open-channel flow. Thus, the study by Lotsari *et al*. (2017) more resembled the study of Attar and Li (2013), who had found the HVC to vary between different cross-sections under ice cover. In the present study, the HVC of the ADCP measurements was located slightly more towards the outer or inner banks (for example, in the downstream parts of Bends 1 and 3) compared to the HVC of the modelled ice-covered flow. Thus, despite the overall good correspondence of the ice-covered model to the measured flow depth, river-ice elevations, depth-averaged flow velocities and the broadscale movement of the HVC, the ice-covered model smoothed the spatial variability of flow. Thus, it was not able to model the cross-sectional peak flow locations in as much detail as the measurements (cf. Lotsari *et al.,* 2017). Regardless of this, the model was able to reproduce the more variable flow directions under the ice next to the banks than in the open-channel flow conditions.

Similar to the present modelling results, earlier studies have shown observations of high velocities in the shallowest areas, for example mid-channel bars both in open-channel conditions (Kang and Sotiropoulos, 2011) and in ice-covered flow conditions (Demers *et al.,* 2011; Lotsari *et al.,* 2017). However, the overall simulated and observed velocities were lower under ice than when the river was open. Note that there was one location at the outer bank of the upstream section of Bend 1 where the ice-covered flow velocities were higher than during the open-channel conditions. This is possibly due to the ice, which narrowed the channel and diverted the flow towards the outer bank of the channel. These higher velocities were also the reason for the channel being open at this location mid-winter in 2014 (Kämäri *et al.,* 2017; Lotsari *et al.,* 2017). The present model results also confirmed that low velocities occurred in deep waters, particularly in the downstream part of each meander bend. One distinct morphological characteristic of the Pulmanki River is that the reach between Bends 1 and 2 differs from the classical view that the reaches between two consecutive bends are shallow (Leopold and Wolman, 1960; Knighton, 1984). This reach was the deepest of the whole study area and velocities were also low. One explanation for this could be the asymmetry of Bend 1, as the curvature of the channel is higher in the downstream part of the bend and the apex does not locate symmetrically in the middle of the bend.

Horizontal RFSs formed in both open-channel and ice-covered flow simulations, similar to observations in earlier studies (Ferguson *et al.,* 2003; Blanckaert, 2010; Demers *et al.,* 2011; Blanckaert *et al.,* 2013). Typically, the formation of the RFSs is enhanced in open-channel flow conditions by the high curvature of bends, slow flow velocities, shallow depths and the widening of the channel (Hodskinson and Ferguson, 1998; Blanckaert, 2010; Blanckaert *et al.,* 2013). In open-channel conditions, only one RFS was clearly caused by the curvature of Pulmanki River. This was located at the downstream part of Bend 1. In addition, the widening of the channel caused one RFS in the straight reach. These results were thus in line with the earlier theories of the formation of the RFSs during open-channel low flow conditions (Hodskinson and Ferguson, 1998; Blanckaert, 2010; Blanckaert *et al.,* 2013). Similar to the open-channel situation, an RFS formed in the straight reach due to the widening of the channel under ice cover. However, in ice-covered conditions, the strongest simulated RFS formed close to the inner bank at the apex of Bend 2, where the depth was shallow, velocities were low and curvature was high. In addition to the widening of the channel in this location, the fact that Bend 2 had the highest overall curvature of the three studied meander bends (cf. Lotsari *et al.,* 2014a) could explain the formation of the RFS. Ice-covered flow simulations did not form RFSs in the downstream part of Bend 1 because the ice had narrowed the channel compared to the open-channel conditions. Because the ice cover itself did not have variation in its roughness characteristics within the study area, the spatial impacts of ice can be considered to relate to its confining effect and not to its roughness.

Blanckaert *et al*. (2013) had noticed that RFSs form in meander bends connected to shallow water bar areas on the inner bank and deep pools on the outer-bank side. Also, in the present study, the formation of RFSs took place in this type of location during both the open-channel and ice-covered flow simulations. The flow direction was diverted towards the banks in these RFS locations (e.g. in Bend 1 during open channel simulations) in a way similar to that shown by the study of Blanckaert *et al*. (2013). Lotsari *et al*. (2017) also observed how flow was directed towards the banks near the shorelines. However, the sparsity of cross-sectional measurements had disabled the detection of horizontal RFSs by Lotsari *et al*. (2017). According to Blanckaert *et al*. (2013), an RFS on the inner bank could also promote the formation of RFSs on the outer bank. The simulation results support this conclusion as there were weaker RFSs at the outer bank of Bend 2 in ice-covered conditions (i.e. in the proximity of the inner bank's stronger RFS). The open-channel simulations did not produce smaller RFSs close to the stronger ones. Thus, based on the model results, ice cover could promote the formation of multiple small, horizontally recirculating RFSs close to the strongest RFS cells next to the banks. All in all, there were more of these horizontal RFSs in the ice-covered simulations.

Thus, the present study revealed differences in the formation of RFS locations between the seasons, but the characteristics of these flow structures and the reasons for their formation were similar in both open-channel and ice-covered flow conditions. However, their formation has not been studied much in ice-covered meander bends (Prowse and Beltaos, 2002), and further studies are encouraged. For example, a study involving denser drilling and measurement network would provide better validation possibilities for model results.

The seasonal erosion–sedimentation potential of a subarctic river

Normally in an open-channel situation, the RFSs on the inner-bank side of the channel, with their slow flow velocities, enable the settling of the sediment (Ferguson *et al.,* 2003; Blanckaert, 2011). Therefore, it is more likely that RFSs promote deposition within these locations, both in open-channel and ice-covered conditions. The large RFS of Bend 1 could thus enhance the asymmetry of Bend 1 in the future if the deposition takes place on this inner-bank side of the channel. In addition, further studies on the importance of sedimentation on the point bars and inner bank areas during ice-covered periods should be performed as the simulated RFS on Bend 2 formed in this type of location.

Turcotte *et al*. (2011) stated that it has not been possible to thoroughly explore the effects of stable ice-cover on the sediment transport capacity of a river channel, even though the transport has been observed to diminish (25–95%) during ice-covered conditions, when compared to open-channel flow. Knack and Shen (2015) showed that it is possible to describe bedload transport in ice-covered channels with conventional relationships for the equivalent free-surface flow. The present study showed that coverage of the areas where critical velocities were exceeded was reduced due to ice cover, based on both simulation and measurement results. Thus, the conditions were more prone to sedimentation during the ice-covered conditions than in the open-channel conditions of the preceding autumn.

Despite these overall differences in flow magnitude, the greatest erosion potential would be expected in the straight reach of Pulmanki River as the actual critical velocities of measured sediment samples were exceeded there in both open-channel and ice-covered conditions. Also, based on the minimum, maximum and average critical velocities, both measured and simulated ice-covered and open-channel flow magnitudes indicate erosion in the straight reach and the upstream part of Bend 1. Thus, the overall erosion potential of the asymmetrical Bend 1 was greater than at the symmetrical Bends 2 and 3. The D_{50} value of the measured bedload in mid-winter conditions of February 2017 (cf. Study Area section) gives confidence in the existence of sediment transport under ice cover. The D_{50} value was between the grain sizes corresponding to the minimum and average critical velocities calculated based on the 22 sediment samples and the Hjulström diagram (1935). This also gives further confidence in the application of the Hjulström method for the analyses of the incipient motion.

The results of erosion–sedimentation potential analyses also indicate that the spatial variability and differences in depositional and erosional locations were increased during ice-covered conditions. Thus, ice cover should be considered as one of the inherent factors – among other factors such as flood duration and the rate of discharge increase and decrease – which cause the rivers and their bends to act differently during both short- and long-term time periods (Kasvi *et al.,* 2017). Even though the short open-channel flow period causes greater flow velocities and related channel changes, the ice-covered flow, which lasts about eight months annually, and evident sediment transport should not be ignored from the analyses of subarctic rivers. The ice-covered high flows concentrated on narrower areas, defined by the ice extents (cf. Kämäri *et al.,* 2017; Lotsari *et al.,* 2017), and the spatial differences in high and low flow locations were increased when compared to open-channel conditions. Thus, the ice-covered period can influence the thalweg locations occurring in the beginning of the next open-channel flow period and therefore also the annual river channel changes. Therefore, we agree with Turcotte *et al*. (2011) that further research is needed on flow characteristics under stable ice-cover conditions and also with higher discharge conditions.

Conclusions

The model enabled analyses from a spatially wider area than analyses that are only based on single cross-sectional measurements. The 2D hydrodynamic simulation approach was well suited for the analyses of the spatial variation of flow characteristics in ice-covered and open-channel conditions. Despite the fact that further tests and analyses of ice-covered flow that are based on different types of models are encouraged, this study enabled new knowledge to be gained about the spatial variation of flow and erosion–sedimentation characteristics of a subarctic river.

Compared to previous studies performed in the same river, the present study showed for the first time how ice cover narrowed the highest flow velocity areas from the open-channel situation. This promoted spatial differences in high and low flow locations in ice-covered conditions. As this subarctic river has ice cover for *c.* 7–8 months annually, these differences in high flow locations may greatly influence the thalweg locations and therefore also the annual river channel evolution.

The horizontal RFSs also formed in different locations depending on whether the river was open or covered with ice. However, the characteristics of the RFSs and the causes for their formation were similar during both conditions: (1) they were caused by the obstacles on the river bed, such as mid-channel bars and the roughness of the banks, (2) part of the RFSs were also caused by the high curvature of the bend and (3) the sudden widening of the bend. The ice, which caused narrowing of the channel, influenced seasonal differences in their occurrence. The ice cover also promoted groups of small RFSs, which were not found during open-channel flow conditions. As the low flow was favourable for deposition in the middle of these RFSs, these flow structures could be important for seasonal differences in channel morphodynamics. Further studies on horizontal RFSs under ice cover are needed, but this present study shows the hypothesis to be correct: the flow characteristics are spatially more variable in ice-covered conditions than during the open-channel conditions.

The findings regarding the exceedance of the critical velocity thresholds indicate spatially extensive sediment transport in open-channel conditions, but the spatial variability and differences in depositional and erosional locations increases during ice-covered conditions. The asymmetrical bend and the straight reach erode throughout the year, whereas smaller symmetrical bends only erode in open-channel conditions and are prone to deposition in winter. Thus, the combined effects of the differences in the spatial occurrence of the high velocities, horizontal RFSs and the exceedance of the critical flow thresholds between the seasons indicate that the long ice-covered season can greatly affect the annual morphological changes (such as bar formation) of the submerged channel.

Acknowledgements—This study is a continuation to the master's thesis research undertaken by Tiia Tarsa, and therefore, it would not have been done without her initial excellent contribution to the simulation approaches. The study was funded by the Academy of Finland ('Extreme and annual fluvial processes in river dynamics – ExRIVER' [grant number 267345]), by the Maj and Tor Nessling Foundation ('*Äärimmäisten ja vuotuisten fluviaaliprosessien vaikutukset jokidynamiikkaan*' [grant numbers 2013067 and 2015046], 'The Influence of River Ice and Fluvial Processes on River Environments Now and in the Future' [grant number 2016042]) and by the Strategic Research Council, the Academy of Finland (COMBAT project [grant number 293389]). The authors thank Claude Flener, Leena Laamanen, Jenni-Mari Vesakoski and Yungsheng Wang from the University of Turku and Antero Kukko, Harri Kaartinen and Anttoni Jaakkola from the Finnish Geospatial Research Institute, National Land Survey of Finland for their help in fieldwork at Pulmanki River. In addition, valuable help in the field was gained from Mikel Calle Navarro (CSIC, Madrid) and Matti Vaaja and Matti Kurkela (Aalto University, Helsinki).

The authors also thank the Kevo subarctic research station for their help with fieldwork and the required equipment. The authors have no conflict of interest to declare.

References

Army US. 1998. *HEC-RAS River Analysis System: Hydraulic Reference Manual*. Hydrologic Engineering Centre, US Army Corps of Engineers: Davis, CA.

Attar S, Li SS. 2013. Momentum, energy and drag coefficients for ice-covered rivers. *River Research and Applications* **29**: 1267–1276. https://doi.org/10.1002/rra.2611.

Barrows HK, Horton RE. 1907. *Determination of Stream Flow During the Frozen Season*, Water-Supply and Irrigation Paper 187, Series M, General Hydrographic Investigations 19. Department of the Interior, United States Geological Survey: Washington, DC.

Beltaos S. 1995. *River Ice Jams*. Water Resources Publications: Littleton, CO; 372.

Beltaos S. 2013. *River Ice Formation*. Committee on River Ice Processes and the Environment: Edmonton; 552.

Blackburn J, Unterschultz K. 2002. *R2D_Ice: Ice Topography File Editor. User's Manual*. University of Alberta: Edmonton.

Blanckaert K. 2010. Topographic steering, flow recirculation, velocity redistribution, and bed topography in sharp meander bends. *Water Resources Research* **46**: 1–23. https://doi.org/10.1029/2009WR008303.

Blanckaert K. 2011. Hydrodynamic processes in sharp meander bends and their morphological implications. *Journal of Geophysical Research: Earth Surface* **116**: 1–22. https://doi.org/10.1029/2010JF001806.

Blanckaert K, Kleinhans MG, McLelland SJ, Uijttewaal WSJ, Murphy BJ, van de Kruijs A, Parsons DR, Chen Q. 2013. Flow separation at the inner (convex) and outer (concave) banks of constant-width and widening open-channel bends. *Earth Surface Processes and Landforms* **38**: 696–716. https://doi.org/10.1002/esp.3324.

Brunner GW. 2010. *HEC-RAS, River Analysis System Hydraulic Reference Manual*. US Army Corps of Engineers, Hydrologic Engineering Center (HEC): Davis, CA.

Demers S, Buffin-Bélanger T, Roy AG. 2011. Helical cell motions in a small ice-covered meander river reach. *River Research and Applications* **27**: 1118–1125. https://doi.org/10.1002/rra.1451.

Demers S, Buffin-Bélanger T, Roy AG. 2013. Macroturbulent coherent structures in an ice-covered river flow using a pulse-coherent acoustic Doppler profiler. *Earth Surface Processes and Landforms* **38**: 937–946. https://doi.org/10.1002/esp.3334.

Dietrich WE, Smith JD. 1983. Influence of the point bar on flow through curved channels. *Water Resources Research* **19**: 1173–1192.

Engel FL, Rhoads BL. 2017. Velocity profiles and the structure of turbulence at the outer bank of a compound meander bend. *Geomorphology* **295**: 191–201. https://doi.org/10.1016/j.geomorph.2017.06.018.

Ettema R. 2002. Review of alluvial-channel responses to river ice. *Journal of Cold Regions Engineering* **16**: 191–217. https://doi.org/10.1061/(ASCE)0887-381X(2002)16:4(191).

Ettema R, Braileanu F, Muste M. 2000. Method for estimating sediment transport in ice-covered channels. *Journal of Cold Regions Engineering* **14**: 130–144.

Ferguson RI, Parsons DR, Lane SN, Hardy RJ. 2003. Flow in meander bends with recirculation at the inner bank. *Water Resources Research* **39**: 1–13. https://doi.org/10.1029/2003WR001965.

Fukuda S, Tanakura T, Hiramatsu K, Harada M. 2015. Assessment of spatial habitat heterogeneity by coupling data-driven habitat suitability models with a 2D hydrodynamic model in small-scale streams. *Ecological Informatics* **29**: 147–155. https://doi.org/10.1016/j.ecoinf.2014.10.003.

Hjulström F. 1935. Studies of morphological activity of rivers as illustrated by the River Fyris. *Bulletin of the Geological Institute University of Uppsala* **25**: 221–527.

Hodskinson A, Ferguson RI. 1998. Numerical modelling of separated flow in river bends: model testing and experimental investigation of geometric controls on the extent of flow separation at the concave bank. *Hydrological Processes* **12**: 1323–1338. https://doi.org/10.1002/(SICI)1099-1085(19980630)12:8<1323::AID-HYP617>3.0.CO;2-S.

Intergovernmental Panel on Climate Change (IPCC). 2013. Summary for policymakers. In *Climate Change 2013: The Physical Science Basis, Contribution of Working Group I to the Fifth Assessment Report of the IPCC*, Stocker TF, Qin D, Plattner G-K, Tignor M, Allen SK, Boschung J, Nauels A, Xia Y, Bex V, Midgley PM (eds). Cambridge University Press: Cambridge; 3–29.

Intergovernmental Panel on Climate Change (IPCC). 2018. Summary for policymakers. In *Global Warming of 1.5°C: An IPCC Special Report on the Impacts of Global Warming of 1.5°C Above Pre-industrial Levels and Related Global Greenhouse Gas Emission Pathways, in the Context of Strengthening the Global Response to the Threat of Climate Change, Sustainable Development, and Efforts to Eradicate Poverty*, Masson-Delmotte V, Zhai P, Pörtner HO, Roberts D, Skea J, Shukla PR, Pirani A, Moufouma-Okia W, Péan C, Pidcock R, Connors S, JBR M, Chen Y, Zhou X, Gomis MI, Lonnoy E, Maycock T, Tignor M, Waterfield T (eds). World Meteorological Organization: Geneva; 1–32.

Kämäri M, Alho P, Aaltonen J, Veijalainen N, Huokuna M, Lotsari E. 2015. River ice cover influence on sediment transportation at present and under projected hydro-climatic conditions. *Hydrological Processes* **29**: 4738–4755. https://doi.org/10.1002/hyp.10522.

Kämäri M, Alho P, Colpaert A, Lotsari E. 2017. Spatial variation of river-ice thickness in a meandering river. *Cold Regions Science and Technology* **137**: 17–29. https://doi.org/10.1016/j.coldregions.2017.01.009.

Kämäri M, Tattari S, Lotsari E, Koskiaho J, Lloyd CEM. 2018. High-frequency monitoring reveals seasonal and event-scale water quality variation in a temporally frozen river. *Journal of Hydrology* **564**: 619–639. https://doi.org/10.1016/j.jhydrol.2018.07.037.

Kang S, Sotiropoulos F. 2011. Flow phenomena and mechanisms in a field-scale experimental meandering channel with a pool-riffle sequence: Insights gained via numerical simulation. *Journal of Geophysical Research* **116**: F03011, 1–22. https://doi.org/10.1029/2010JF001814.

Kasvi E, Alho P, Lotsari E, Wang Y, Kukko A, Hyyppä H, Hyyppä J. 2015. Two-dimensional and three-dimensional computational models in hydrodynamic and morphodynamic reconstructions of a river bend: sensitivity and functionality. *Hydrological Processes* **29**: 1604–1629. https://doi.org/10.1002/hyp.10277.

Kasvi E, Alho P, Vaaja M, Hyyppä H, Hyyppä J. 2013a. Spatial and temporal distribution of fluvio-morphological processes on a meander point bar during a flood event. *Hydrology Research* **44**: 1022–1039. https://doi.org/10.2166/nh.2013.091.

Kasvi E, Laamanen L, Lotsari E, Alho P. 2017. Flow patterns and morphological changes in a sandy meander bend during a flood – spatially and temporally intensive ADCP measurement approach. *Water* **9**: 106. https://doi.org/10.3390/w9020106.

Kasvi E, Vaaja M, Alho P, Hyyppä H, Hyyppä J, Kaartinen H, Kukko A. 2013b. Morphological changes on meander point bars associated with flow structure at different discharges. *Earth Surface Processes and Landforms* **38**: 577–590. https://doi.org/10.1002/esp.3303.

Khelifa A, Hill PS. 2006. Models for effective density and settling velocity of flocs. *Journal of Hydraulic Research* **44**: 390–401. https://doi.org/10.1080/00221686.2006.9521690.

Knack I, Shen H. 2015. Sediment transport in ice-covered channels. *International Journal of Sediment Research* **30**: 63–67. https://doi.org/10.1016/S1001-6279(15)60006-3.

Knighton D. 1984. *Fluvial Forms and Processes*. Edward Arnold: London.

Lal AMW, Shen HT. 1991. A mathematical model for river ice processes. *Journal of Hydraulic Engineering* **117**: 851–867. https://doi.org/10.1061/(ASCE)0733-9429(1991)117:7(851).

Lamb MP, Dietrich WE, Venditti JG. 2008. Is the critical Shields stress for incipient sediment motion dependent on channel-bed slope? *Journal of Geophysical Research* **113**: F02008. https://doi.org/10.1029/2007JF000831.

Lau Y, Krishnappan B. 1985. Sediment transport under ice cover. *Journal of Hydraulic Engineering* **111**: 934–950. https://doi.org/10.1061/(ASCE)0733-9429(1985)111:6(934).

Leopold LB, Wolman MG. 1960. River meanders. *Bulletin of the Geological Society of America* **71**: 769–794.

Lind L, Nilson C, Weber C. 2014. Effects of ice and floods on vegetation in streams in cold regions: implications for climate change. *Ecology and Evolution* **4**: 4173–4184. https://doi.org/10.1002/ece3.1283.

Lotsari E, Kasvi E, Kämäri M, Alho P. 2017. The effects of ice-cover on flow characteristics in a subarctic meandering river. *Earth Surface Processes and Landforms* **42**: 1195–1212. https://doi.org/10.1002/esp.4089.

Lotsari E, Vaaja M, Flener C, Kaartinen H, Kukko A, Kasvi E, Hyyppä H, Hyyppä J, Alho P. 2014a. Annual bank and point bar morphodynamics of a meandering river determined by high-accuracy multitemporal laser scanning and flow data. *Water Resources Research* **50**: 5532–5559. https://doi.org/10.1002/2013WR014106.

Lotsari E, Wainwright D, Corner GD, Alho P, Käyhkö J. 2014b. Surveyed and modelled one-year morphodynamics in the braided lower Tana River. *Hydrological Processes* **28**: 2685–2716. https://doi.org/10.1002/hyp.9750.

Lotsari E, Wang Y, Kaartinen H, Jaakkola A, Kukko A, Vaaja M, Hyyppä H, Hyyppä J, Alho P. 2015. Gravel transport by ice in a subarctic river from accurate laser scanning. *Geomorphology* **246**: 113–122. https://doi.org/10.1016/j.geomorph.2015.06.009.

Magnuson JJ, Robertson DM, Benson BJ, Wynne RH, Livingstone DM, Arai T, Assel RA, Barry RG, Card V, Kuusisto E, Granin NG, Prowse TD, Stewart KM, Vuglinski VS. 2000. Historical trends in lake and river ice cover in the Northern Hemisphere. *Science* **289**: 1743–1746. https://doi.org/10.1126/science.289.5485.1743.

Mansikkaniemi H, Mäki O-P. 1990. Palaeochannels and recent changes in the Pulmankijoki valley, northern Lapland. *Fennia* **168**(2): 137–152.

Prowse TD, Beltaos S. 2002. Climatic control of river-ice hydrology: a review. *Hydrological Processes* **16**: 805–822.

Sayre WW, Song GB. 1979. *Effects of Ice Covers on Alluvial Channel Flow and Sediment Transport Processes*. Iowa Institute of Hydraulic Research: Iowa city, IA.

Shapiro SS, Wilk MB. 1965. An analysis of variance test for normality (complete samples). *Biometrika* **52**: 591–611.

Shields A. 1936. *Anwendung der Aehnlichkeitsmechanik und der Turbulenzforschung auf die Geschiebebewegung*. Mitteilungen der Preußischen Versuchsanstalt für Wasserbau und Schiffbau: Berlin; 26.

Simões JM. 2014. Shear velocity criterion for incipient motion of sediment. *Water Science and Engineering* **7**: 183–193. https://doi.org/10.3882/j.issn.1674-2370.2014.02.006.

Smith BT, Ettema R. 1995. Ice-cover influence on flow and bedload transport in dune-bed channels. In *IIHR Technical Report 374*. Iowa Institute of Hydraulic Research (IIHR), The University of Iowa: Iowa City, IA.

Sontek. 2018. RiverSurveyor S5 and M9. Web page: https://www.sontek.com/riversurveyor-s5-m9 [16 February 2018].

Steffler P, Blackburn J. 2002. *River2D: Two-dimensional Depth Averaged Model of River Hydrodynamics and Fish Habitat. Introduction to Depth Averaged Modeling and User's Manual*. University of Alberta: Edmonton.

Sui J, Wang J, Balachandar R, Sun Z, Wang D. 2008. Accumulation of frazil ice along a river bend. *Canadian Journal of Civil Engineering* **35**: 158–169. https://doi.org/10.1139/L07-093.

Sui J, Wang J, He Y, Krol F. 2010. Velocity profiles and incipient motion of frazil particles under ice cover. *International Journal of Sediment Research* **25**: 39–51. https://doi.org/10.1016/S1001-6279(10)60026-1.

Tan C-A, Sinha S, Ettema R. 1998. Numerical simulation of near-field mixing in ice-covered channels. In *IIHR Technical Report No. 391*. Iowa Institute of Hydraulic Research (IIHR), College of Engineering, The University of Iowa: Iowa City, IA.

Tsai W-F, Ettema R. 1994. Ice cover influence on transverse bed slopes in a curved alluvial channel. *Journal of Hydraulic Research* **32**: 561–581. https://doi.org/10.1080/00221686.1994.9728355.

Tsai W-F, Ettema R. 1996. A study of ice-covered flow in an alluvial bend. In *IIHR Report No. 376*. Iowa Institute of Hydraulic Research (IIHR), College of Engineering, The University of Iowa: Iowa City, IA.

Turcotte B, Morse B. 2017. The winter environmental continuum of two watersheds. *Water* **9**: 337. https://doi.org/10.3390/w9050337.

Turcotte B, Morse B, Bergeron NE, Roy AG. 2011. Sediment transport in ice-affected rivers. *Journal of Hydrology* **409**: 561–577. https://doi.org/10.1016/j.jhydrol.2011.08.009.

Urroz GE, Ettema R. 1994. Application of two-layer hypothesis to fully developed flow in ice-covered curved channels. *Canadian Journal of Civil Engineering* **21**: 101–110. https://doi.org/10.1139/l94-010.

Vaaja M, Hyyppä J, Kukko A, Kaartinen H, Hyyppä H, Alho P. 2011. Mapping topography changes and elevation accuracies using a mobile laser scanner. *Remote Sensing* **3**: 587–600. https://doi.org/10.3390/rs3030587.

Vietz GJ, Rutherfurd ID, Stewardson MJ, Finlayson BL. 2012. Hydrodynamics and sedimentology of concave benches in a lowland river. *Geomorphology* **147**: 86–101. https://doi.org/10.1016/j.geomorph.2011.07.033.

Waddle T. 2007. *Simulation of Flow and Habitat Conditions Under Ice, Cache la Poudre River – January 2006*, Open-File Report 2007-1282. US Department of the Interior, US Geological Survey: Reston, VA.

Wang J, Sui J, Karne BW. 2008. Incipient motion of non-cohesive sediment under ice cover – an experimental study. *Journal of Hydrodynamics* **20**: 117–124. https://doi.org/10.1016/S1001-6058(08)60036-0.

Wang J, Li Q, Sui J. 2010. Floating rate of frazil ice particles in flowing water in bend channels – a three-dimensional numerical analysis. *Journal of Hydrodynamics, Ser. B* **22**: 19–28. https://doi.org/10.1016/S1001-6058(09)60023-8.

Wang J, Chen P, Sui J. 2011. Progress in studies on ice accumulation in river bends. *Journal of Hydrodynamics* **23**: 737–744. https://doi.org/10.1016/S1001-6058(10)60171-0.

Wilcox RR. 2009. *Basic statistics: Understanding conventional methods and modern insights*. Oxford University Press: New York.

Yapa PD, Shen HT. 1986. Unsteady flow simulation for an ice-covered river. *Journal of Hydraulic Engineering* **112**: 1036–1049. https://doi.org/10.1061/(ASCE)0733-9429(1986)112:11(1036).